

Atmospheric rRivers in CMIP5 climate ensembles downscaled with a high resolution regional climate model

Matthias Gröger¹, Christian Dieterich^{1†}, Cyril Duteuil¹, H.E. Markus Meier^{1,2}, Dmitry V. Sein^{3,4},

¹Department of Physical Oceanography and Instrumentation, Leibniz Institute for Baltic Sea Research

5 Warnemünde, Rostock, 18119, Germany

²Research and Development Department, Swedish Meteorological and Hydrological Institute, Norrköping, 601 76, Sweden

³ Shirshov Institute of Oceanology, Russian Academy of Sciences; Moscow, Russia

⁴ Alfred Wegener Institute, Helmholtz Centre for Polar and Marine Research; Bremerhaven, Germany

10 † [deceased](#)

Correspondence to: Matthias Gröger (matthias.groeger@io-warnemuende.de)

Abstract

15 Atmospheric rivers (AR) are important drivers of heavy precipitation events in western and central Europe and often associated with intense floods. So far, the ARs response to climate change in Europe has been investigated by global climate models within the CMIP5 framework. However, their spatial resolution between 1 and 3° is too coarse for an adequate assessment of local to regional precipitation patterns. Using a regional climate model with 0.22° resolution we downscale an ensemble of 24 global climate simulations following the greenhouse gas scenarios RCP2.6, RCP4.5, RCP8.5. Atmospheric rivers (AR) are important drivers of hazardous precipitation levels and are often associated with intense floods. So far, the response of ARs to climate change in Europe has been investigated using global climate models within the CMIP5 framework. However, the spatial resolution of those models (1–3°) is too coarse for an adequate assessment of local to regional precipitation patterns. Using a regional climate model with 0.22° resolution, we downscaled an ensemble of 24 global climate simulations following greenhouse gas emission scenarios RCP2.6, RCP4.5, RCP8.5.

30 The performance of the climate model to simulate AR frequencies and AR induced precipitation was tested against ERA-I reanalysis data. Overall, we find a good agreement between the downscaled CMIP5 historical simulations and ERAI. The downscaled simulation notably better represents small-scale spatial characteristics. However, the downscaled simulations better represented small-scale spatial characteristics, which is most obvious over the terrain of the Iberian Peninsula where the AR-induced precipitation pattern clearly reflect east-west striking topographical elements resulting in zonal bands of high and low AR impact. This was most evident over the terrain of the Iberian Peninsula, where the AR-induced precipitation pattern clearly reflected prominent east-west topographical elements, resulting in zonal bands of high and low AR impact. Over central Europe the model simulates a less far propagation of ARs toward eastern Europe compared to ERA-I. Over central Europe, the models simulated a smaller propagation distance of AR toward eastern Europe than obtained using the ERAI data, but a higher share of AR forced heavy precipitation events especially Norway where 60% of annual precipitation maxima are related to ARs.

45 We find ARs more frequent and more intense in a future warmer climate especially in the higher emission scenarios whereas the changes are mostly mitigated under the assumption of RCP2.6. They also propagate further inland to eastern Europe in a warmer climate. In the high emission scenario

RCP8.5 AR-induced precipitation rates increase between 20 and 40% in western-central Europe while mean precipitation rates increase by maximal 12%. Over the Iberian Peninsula AR-induced precipitation rates slightly decrease around 6% but mean rates decrease around 15%.

The result of these changes is an overall increased contribution of ARs to heavy precipitation with greatest impact over Iberia (15–30%). Our models showed that AR in a future warmer climate will be more frequent and more intense, especially in the higher-emission scenarios (RCP4.5, RCP8.5). However, assuming low emissions (RCP2.6), the related changes can be mostly mitigated. According to the high-emission scenario RCP8.5, AR-induced precipitation will increase by 20–40% in western central Europe, whereas mean precipitation rates increase by a maximum of only 12%. Over the Iberian Peninsula, AR-induced precipitation will slightly decrease (~6%) but the decrease in the mean rate will be larger (~15%). These changes will lead to an overall increased fractional contribution of AR to heavy precipitation, with the greatest impact over Iberia (15–30%) and western France (~15%). Likewise, the fractional share of yearly maximum precipitation attributable to AR will increase over Iberia, the UK, and western France.

Over Norway average AR precipitation rates decline between 5 to 30%. These reductions most likely originate from regional dynamical changes. In fact, over Norway we find ARs originating from >60°N are reduced by up to 20% while those originating south of 45°N are increased. Over Norway, average AR precipitation rates will decline by 5 to 30%, most likely due to dynamic changes, with AR originating from latitudes >60°N decreasing by up to 20% and those originating south of 45°N increasing. This suggests that AR over Norway will follow longer routes over the continent, such that additional moisture uptake will be impeded. By contrast, AR from >60°N will take up moisture from the North Atlantic before making landfall over Norway. Also, no clear climate change signal is seen for AR-related heavy precipitation and annual maximum precipitation over Norway where the uncertainty of the ensemble is quite large.

1 Introduction

Atmospheric rivers (ARs) are long and narrow corridors that transport large amounts of moisture from tropical and subtropical origin poleward (e.g. Zhu et al., 1998; Gimeno et al., 2014; Gimeno et al., 2016; Shields et al., 2019). On the other hand AR induced heavy precipitation can likewise cause tremendous economical damage due to flooding (e.g. Gimeno et al., 2016; Payne et al., 2020).

Massoud et al., 2020 (Middle East or North Africa) play an important role for the local water management (Lavers and Villarini, 2015; Gimeno et al., 2016), for example in dry areas of the and to be a strong contributor to the local groundwater inventory in regions prone to droughts. Associated with intense precipitation they can. Due to their intense moisture load they play an important role for the global water cycle. It has been estimated that ARs are responsible for >90% of the meridional moisture transport through the mid-latitudes (e.g. Gimeno et al., 2016, Gimeno et al., 2018). ARs are associated with extraordinary strong low-level winds often positioned at the head of a cold front of extra-tropical storm systems (e.g. Dacre et al., 2015; Gimeno et al., 2016). Accordingly, they are modulated by large scale weather regimes as demonstrated by Pasquier et al. (2019). In the North Atlantic sector the moisture source for ARs originates mainly from the subtropical Atlantic (Ramos et al., 2016). ARs can occur during the whole year but due to their strong linkage to extra-tropical storm systems they are more frequent during the cold season in the Northern Hemisphere (Lavers and Villarini 2013; Ramos et al., 2015). Atmospheric rivers (AR) are long, narrow corridors that transport enormous amounts of moisture from tropical and subtropical origins poleward (e.g., Zhu et al., 1998; Gimeno et al., 2014; Gimeno et al., 2016; Shields et al., 2019). Due to their intense moisture loads, they play an important role in the global water cycle. It has been estimated that AR are responsible for >90% of meridional moisture transport through mid-latitudes (e.g., Gimeno et al., 2016, Gimeno et al., 2018). In addition, AR are associated with very powerful low-level winds often positioned at the head

95 of a cold front of an extra-tropical storm system (e.g., Dacre et al., 2015; Gimeno et al., 2016).
Accordingly, they are modulated by large-scale weather regimes, as demonstrated by Pasquier et al.
(2019). In the North Atlantic sector, the moisture contained in AR originates mainly from the
subtropical Atlantic (Ramos et al., 2016a). Although AR can occur throughout the year, due to their
100 strong linkage to extra-tropical storm systems they are more frequent during the cold season in the
Northern Hemisphere (Lavers and Villarini 2013; Ramos et al., 2015).

In the North Atlantic and North Pacific, AR pose a serious risk of heavy precipitation and flooding
along the western coasts of California and Europe (e.g., Ralph et al., 2006; Neiman et al., 2011;
105 Ralph and Dettinger, 2012; Lavers et al., 2011, Lavers et al., 2012; Lavers and Villarini; 2013; Ramos
et al. 2015; Gao et al., 2016, Nayak et al., 2016; Nayak et al., 2017). Flooding is expected to increase
under a warming climate, incurring high economic costs as well (Ashley et al., 2005; Sayers et al.,
2015; Alfieri et al., 2016). Elucidation of the mechanisms that give rise to AR and thus to an increased
flood risk is therefore essential to mitigate their impact (e.g., Kouski 2014; Alfieri et al., 2018).

110 In the North Atlantic and North-Pacific Sectors of the World Ocean ARs have been identified as a big-
risk for heavy precipitation and flooding along the western coasts of California and Europe (e.g. Ralph
et al., 2006; Neiman et al., 2011; Ralph and Dettinger, 2012; Lavers et al., 2011, Lavers et al., 2012;
Lavers and Villarini; 2013; Ramos et al. 2015; Gao et al., 2016, Nayak et al., 2016; Nayak et al.,
115 2017). In Europe flooding causes large amounts of economic damages which is expected to increase
under climate warming (Ashley et al., 2005; Sayers et al., 2015; Alfieri et al., 2016). Therefore, it is
essential to investigate mechanisms that rise the risk for floods (e.g. Kouski 2014; Alfieri et al., 2018).
For Europe a significant role of ARs in heavy precipitation events and flooding has been
demonstrated by previous studies. Lavers and Villarini (2013) analyzed atmospheric reanalysis data
sets and found up to 8 out of the 10 annual maximum precipitation events to be related to ARs during
120 the period 1979-2011. Several studies have examined heavy precipitation events and flooding in
Europe attributable to AR. For example, Lavers and Villarini (2013) analyzed atmospheric reanalysis
data and found that between 1979 and 2011 as many as eight of the ten annual maximum
precipitation events were related to AR. In Europe, most damage associated with AR occurs along the
western continental margin, especially over the Iberian Peninsula, the UK, and Scandinavia (Lavers et
125 al. 2013, Ramos et al., 2015; Whan et al., 2020). However, AR can also penetrate far inland,
producing heavy rainfall events as far east as Germany and Poland (Lavers and Villarini, 2013, Ionita
et al., 2020). Unlike the heavy precipitation events associated with the local formation of short-lived
convective cells during summer, AR typically produce hazardous precipitation continuously over
several days (Shields and Kiehl, 2016). Nonetheless, with their intense precipitation, AR also strongly
130 contribute to local groundwater management. In dry and semi-arid regions, they can play an important
role in local water groundwater recharge and the irrigation of dry land vegetation (Albano et al.,
2017;) as is the case in many regions around the Mediterranean (Martos-Rosillo et al., 2015).

135 In Europe most damages associated with ARs are located along the western continental margins in
particular over the Iberian Peninsula, the United Kingdom (UK) and Scandinavia (Laver et al. 2013,
Ramos et al., 2015; Whan et al., 2020). However they also can penetrate far inland and produce
heavy rainfall events as far east as in Germany and Poland (Lavers and Villarini, 2013).contribute
significant amounts of precipitation to the annual total precipitation especially in semi-arid regions and
140 thus can be an important source to the local water inventory in regions often threatened by droughts
(e.g. Laver and Villarini, 2015; Ramos et al., 2016; Gimeno et al., 2016). Besides their potential to
force flooding ARs can
Because of the larger water holding capacity of a warmer atmosphere it has been suggested that
climate warming will increase the risk for intense flooding (e.g. Held and Soden ,2006). Lavers et al.
(2015) demonstrated that the intensification of the global water cycle due to climate warming

145 strengthens the mean atmospheric water transports over the North Atlantic by 30—40%. So far,
assessments of AR related flood risk in a future warmer climate are primarily based on climate
projections from global climate models (e.g. Lavers et al., 2013; Lavers et al., 2015; Warner et al.,
2015, Ramos et al., 2016; Gao et al., 2016; Espinoza et al., 2018; Whan et al., 2020). Lavers et al.
150 (2013) showed an intensification of AR in terms of frequency and intensity in future climate based on
the analysis of five CMIP5 global models. Ramos et al. (2016) found a doubling of AR frequency
together with an increase of moisture load in the RCP4.5 and RCP8.5 scenarios in six CMIP5 models
at the end of the 21st century compared to the historical period. Gao et al. (2016) analyzed an
ensemble of 24 CMIP5 global models and found a pronounced increase in the contribution of AR
155 related precipitation to the total annual precipitation in a future warmer climate following the RCP8.5-
scenario. Whan et al. (2020) recently used the high resolution version of the CMIP5 EC-Earth model
to study the climate change impact on AR induced precipitation over Norway. They indicated that up
to 80% of the winter maximum precipitation is associated with ARs. They also found the magnitude of
extreme precipitation events to be mainly controlled by AR intensity. Because of the larger water-
holding capacity characteristic of a warmer atmosphere, climate warming is expected to increase the
160 risk of intense flooding (e.g., Held and Soden, 2006). Lavers et al. (2015) demonstrated that an
intensification of the global water cycle due to climate warming will strengthen the mean transport rate
of atmospheric water over the North Atlantic by 30–40%. So far, assessments of AR in a future
warmer climate have been primarily based on climate projections from global models (e.g., Lavers et
al., 2013; Warner et al., 2015, Ramos et al., 2016; Gao et al., 2016; Espinoza et al., 2018; Whan et
165 al., 2020). For example, Lavers et al. (2013) analyzed five global models from the Couple Model
Intercomparison Project (CMIP5, Taylor et al., 2012) and found an intensification of AR in terms of
their frequency and moisture load in a future climate. Based on the RCP4.5 and RCP8.5 scenarios,
Ramos et al. (2016) determined a doubling of AR frequency together with an increased moisture load
at the end of the 21st century compared to the historical period. Gao et al. (2016) analyzed an
170 ensemble of 24 CMIP5 global models and found a pronounced increase in the fractional contribution
of AR-induced precipitation to the total annual precipitation, based on global projections following the
RCP8.5 scenario. Whan et al. (2020) used the high-resolution version of the CMIP5 EC-Earth model
to study the impact of climate change on AR-induced precipitation over Norway. Up to 80% of the
winter maximum precipitation was shown to be associated with ARs. The authors also found that the
175 magnitude of extreme precipitation events is mainly controlled by AR intensity.

The aforementioned studies analyzed global models from the CMIP5 and CMIP6 frameworks, in
which the spatial resolution typically ranges from 1° to 3°. This resolution is sufficient to assess the
180 large-scale impact of climate on precipitation but it is unable to fully resolve small scale characteristics
such as small convective cells (Hoheneger et al., 2020; Stevens et al., 2020). A further shortcoming of
global models is their poor representation of orography, which in both CMIP5 and CMIP6 is typically
lower than in the real world and thus leads to the over-simplifications of modeled processes (Baldwin
et al., 2021) associated with, e.g., the uplift or blockage of an air mass. While high-resolution climate
185 models covering a limited region largely settle these issues, regional model assessments that focus
on AR are still lacking for Europe. Therefore, in this study, a high-resolution regional climate model for
Europe was employed to downscale global climate simulations derived from the CMIP5 suite.

Purpose of this study

190 ° to 3° allowing a robust analysis of the large scale impact on continental scale precipitation. However,
they do not fully resolve small scale characteristics which is necessary to assess the local impact on
AR related precipitation patterns. provide a resolution typically ranging from 1 employed The majority
of global models currently employed in the CMIP5 and CMIP6 framework The main purposes of this

study are to:

- conduct the first analysis of AR over Europe using a downscaled CMIP5 model ensemble
- investigate the added value of high resolution in representing AR in a climate model.
- assess future climate related changes in AR characteristics over Europe.
- explore uncertainties with respect to the choice of the global model and in regard to the choice of the greenhouse gas (GHG) emission scenario.

For Europe such regional assessments are still lacking.

Here, we investigate how far downscaled high resolution regional projections can improve the representation of ARs on the regional scale and thus add value to global assessments.

Here in the following, we present the first analysis of AR in a regional climate ensemble for Europe based on a horizontal resolution of 0.22° . The ensemble was used to examine future changes in AR frequency and AR-induced heavy precipitation patterns over Europe as well as the impact of AR on the local water budget. Climate-induced changes in the pathways of AR on their journey across Europe were analyzed. Finally, uncertainties with respect to three different climate scenarios (RCP2.6, RCP4.5, RCP8.5) and nine different parent global climate models from the CMIP5 suite were assessed.

We analyze for the first time a regional climate ensemble for Europe based on a horizontal resolution of 0.22° . We use this ensemble to analyze future changes in AR frequency and AR-induced heavy precipitation pattern over Europe and their implication for the local water budget. We likewise aim to assess climate-induced changes in the regional pathways of ARs on their journey across Europe. Finally, we assess uncertainties with respect to 3 different climate scenarios (RCP2.6, RCP4.5, RCP8.5) and 9 different global climate models from the CMIP5 suite.

The paper is outlined as followed: Section 2 briefly describes the regional climate model RCA-NEMO as well the AR detection procedure. Section 3 provides a validation and investigates the added value of high resolution for the present-day period RCA historical ensemble with respect to ARs. Section 4 analyzes future changes in AR frequencies and the impact on precipitation under different climate scenarios. Section 5 discusses uncertainties with respect to the choice of the driving global model. Main conclusions are summarized in section 6. The paper is structured as follows: Section 2 briefly presents the regional climate model (RCA) and the AR detection procedure. Section 3 describes the validation of the climate model, based on a comparison of downscaled CMIP5 historical simulations with ERAI reanalysis data. The added value of a high resolution is demonstrated by downscaling the ERAI reanalysis (Dee et al., 2011) from 0.75° resolution to 0.22° using the high-resolution model RCA. Section 4 analyzes future changes in AR frequencies and the impact on precipitation under different climate scenarios. Section 5 discusses uncertainties with respect to the choice of the driving global model. Our main conclusions make up Section 6.

2. Methods

2.1. The regional climate model RCA-NEMO

The regional climate model (Wang et al., 2015; Gröger et al., 2015; Dieterich et al., 2019) was the Rossby Center regional atmosphere model RCA (Samuelsson et al., 2011; Kupiainen et al., 2014) version 4. RCA was set up for the Euro-Cordex domain (Fig. 1). The horizontal resolution is 0.22° on

240 a rotated grid, which results in a metric resolution of ~24 km (Table 1). The vertical resolution is given
 by 40 hybrid levels. At the lateral boundaries, the model is driven either by reanalysis data (ERA-Interim, Dee
 et al., 2011) or global climate model output. Hence, there is no feedback from the RCA to outside the
 model domain. This means that AR enter the model domain from the parent global model but then
 245 develop freely and independently of the model. The forcing data are prescribed at 6-hourly time
 intervals. The regional climate model (Wang et al., 2015; Gröger et al., 2015; Dieterich et al., 2019)
 consists of the Rossby Center regional atmosphere model RCA (Samuelsson et al., 2011; Kupiainen
 et al., 2014) version 4 coupled to the Ocean General Circulation model NEMO (Table 1, Nucleus for
 European Modelling the Ocean NEMO, Madec, 2012). RCA is a hydrostatic atmosphere model which
 250 is set up for this study according to the Euro-Cordex domain (Fig. 1). The horizontal resolution is 0.22-
 degrees on a rotated grid yielding grid cell sizes between 550–600 km² (Table 1) and the vertical-
 discretization is given by 40 hybrid levels. At the lateral boundaries the model is driven by data from
 either reanalysis data sets or global climate model output. The forcing data are prescribed at 6-hourly
 time intervals.

255 The land surface boundary is prescribed by ECOCLIMAP (Champeaux et al., 2005) and used to
 calculate the land–air mass and energy fluxes. Different to the majority of the EURO-Cordex high-
 resolution ensembles (Jacob et al., 2014), RCA is interactively coupled to the 3D ocean model
 NEMO. The land-surface boundary is defined according to ECOCLIMAP (Champeaux et al., 2005) and
 used to calculate mass and energy fluxes between the Earth’s surface and the atmosphere. Over the
 260 North Sea and Baltic Sea, RCA is interactively coupled to the 3D ocean model NEMO (Nucleus for
 European Modelling the Ocean NEMO, Madec, 2012, Fig. 1, Table 1). The coupling area comprises
 the North Sea and the Baltic Sea. Over this region sea ice temperature, sea ice fraction, sea ice
 albedo, and water temperature is explicitly modeled by NEMO and communicated at 3-h time steps to
 RCA. Air–sea mass and energy fluxes are then calculated in the atmosphere model and used to
 265 drive NEMO which is set up in a resolution of 2 nautical miles (~3.7 km) and 56 vertical varying z*-
 layers. The coupling is managed by the OASIS coupler (Valcke et al., 2003). Outside the coupled
 domain, i.e. the Mediterranean and the North Atlantic, RCA is driven by reanalyses data in the
 hindcast case or by global climate model output. Sea ice temperature, sea ice fraction, sea ice albedo,
 and water temperature over this region are explicitly modeled by NEMO. Air–sea mass and energy
 270 fluxes are then calculated in the atmosphere model and used to drive NEMO, which is set up at a
 resolution of 2 nautical miles (~3.7 km) and 56 vertical varying z* layers. Coupling is managed by the
 OASIS coupler (Valcke et al., 2003). However, with its high resolution and short time stepping, NEMO
 is very expensive to run. Therefore, outside the coupled domain, i.e., the Mediterranean and North
 Atlantic, RCA is driven by reanalysis data or global climate model output. Sea ice fields are explicitly
 275 modeled by the Louvain-la-Neuve sea ice model LIM3 (Vancoppenolle et al., 2008).

Model system	Atmosphere component	Ocean component	Domain size Atmosphere	Domain size ocean model	Grid resolution atmosphere	Vertical levels	Temporal resolution
RCA-NEMO	RCA	NEMO3.3.1	Euro-Cordex	North Sea, Baltic Sea	0.22° (~24x24 km) 550-600 km ²	40	6 hours
ERA-Interim	IFS (Cy31r2)	Prescribed SSTs	global	global	0.75° (806400x45 km) ²	60	6 hours

Table 1: Climate model configuration employed in this study. Also shown is the analyzed data set from the ERA-Interim reanalysis. The climate model RCA configuration employed in this study. The analyzed data set from the ERA-Interim reanalysis is also shown (Dee et al., 2011).

RCA-NEMO has been intensively validated and comprehensively described in detail (e.g. Wang et al., 2015; Gröger et al., 2015; Dieterich et al., 2019; Gröger et al., 2019; Gröger et al., 2021a). It has been employed in large ensembles to study the present climate and to simulate the mean response to

280 global climate change by downscaling global climate scenarios in a huge ensemble (Dieterich et al.,
2019; Gröger et al., 2019; Gröger et al., 2021a). Gröger et al. (2021a) showed that the RCA-NEMO
coupled ensemble is well within the range of the high resolution Euro-Cordex ensemble (Jacob et al.,
2014). However, significant differences arise over interactively coupled areas over sea (Gröger et al.,
2021a; Gröger et al., 2021b). This applies to both climatic mean changes, as well as climatic
285 extremes (e.g. dry periods cold spells, heat waves etc).

The climate model RCA has been intensively validated and comprehensively described (e.g., Wang et
al., 2015; Gröger et al., 2015; Dieterich et al., 2019; Gröger et al., 2019; Gröger et al., 2021a). It has
been employed in previous studies to investigate the present climate and simulate the mean response
290 to global climate change by downscaling global climate scenarios (Dieterich et al., 2019; Gröger et al.,
2019; Gröger et al., 2021a). Gröger et al. (2021a) showed that the RCA-NEMO coupled ensemble is
well within the range of the high-resolution Euro-Cordex ensemble (Jacob et al., 2014). However,
significant differences arise for interactively coupled areas over the sea (Gröger et al., 2021a; Gröger
et al., 2021b). This applies to both climatic mean changes and climatic extremes (e.g., dry periods
295 cold spells, heat waves).

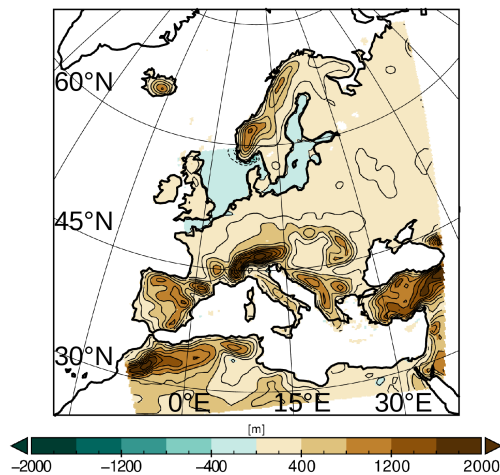


Figure 1: Model domain showing the land topography of the RCA-NEMO climate model (in shades of brown). Bathymetry information indicates the domain of the interactively coupled ocean model NEMO is within the domain of the interactively coupled ocean model NEMO (in shades of blue).

2.2 The high-resolution climate ensemble

300 The above-described model was used to downscale a set of global model climate scenarios taken
from the CMIP5 suite. The above-described model was used to downscale a suite of global model
climate scenarios taken from the Coupled Model Intercomparison Project phase 5 (CMIP5, Taylor et
al., 2012). Table 2 lists the individual realizations and primarily distinguishes the applied scenarios
(first row) and individual model configurations (first column). lists the downscaled RCA simulations as
305 well as the applied scenarios (first row) and individual model configurations (first column).
reanalysis data to validate the model for the present day climate (1979-2009) of the ensemble is

provided by RCA which comprises 34 runs including one ERAI hindcast run. ERA-Interim in addition to the used global climate models we also analyze a hindcast simulation forced by

310

Reg. Model – Glob. model	Historical (1970-1999)	RCP2.6	RCP4.5	RCP8.5
RCA – CANESM2MPI-ESM-LR	x	x	x	x
RCA – CNRM-CM5THEC-EAR	x	x	x	x
RCA – EC-EarthHadGEM2-ES	x	x	x	x
RCA – GFDL-ESM2MIPSL-CM5A-MR	x	x	x	x
RCA – HadGEM2-ESGFDL-ESM2M	x	x	x	x
RCA – IPSL-CM5A-MR-CanESM2	x		x	x
RCA – MIROC5M-CM5CNR	x	x	x	x
RCA – MPI-ESM-LRNorESM1-M	x	x	x	x
RCA – NorESM1-MMIROC5	x	x	x	x
Hindcast period	(1979-2008)			
RCA – ERAI	x			
ERAI – (ECMWF-IFS)	x			

Table 2: Overview of the 34 regional RCA simulations grouped by GHG emission scenarios and downscaled global models. For validation purposes, an RCA-ERAI hindcast was carried out for subsequent comparison with the original ERAI hindcast data set. Due to technical issues, RCP2.6 scenarios for RCA – IPSL-CM5A-MR, RCA – CanESM2, and RCA – CNRM-CM5 could not be performed.

List of 34 coupled regional simulations grouped by greenhouse gas scenarios and downscaled global models:-

315

The chosen climate scenarios follow the protocol of Representative Concentration Pathways (RCP) used in CMIP5 and comprise three different greenhouse gas assumptions. One low emission scenario assumes vigorous mitigation actions (RCP2.6 van Vuuren et al. 2007, 2011) and was developed in regard to limit the global mean temperature to 2 °C warming since the pre-industrial period. It

320

assumes negative emission during the last decade of the 21st century. RCP4.5 is a moderate scenario where emissions peak at the mid-century (2040) and are kept constant after ~2080 at a value about half of the value at the end of the historical period (Clarke et al. 2007; Thomson et al. 2011). Finally, a totally unmitigated scenario RCP8.5 (Riahi et al. 2007; Riahi et al., 2011) assumes rising emissions up to the end of the century. The three scenarios impose a maximal radiative forcing of 2.6, 4.5, and 8.5 W/m² compared to pre-industrial conditions. The chosen climate scenarios follow the protocol of

325

the Representative Concentration Pathways (RCP) used in CMIP5 and derive from three different GHG emission assumptions. The low-emission scenario RCP2.6 assumes both vigorous mitigation actions (van Vuuren et al. 2007, 2011) to limit the global mean temperature increase to +2°C compared to the pre-industrial period and negative emissions during the last decade of the 21st century. RCP4.5 is a moderate-emission scenario in which emissions peak at mid-century (2040) and remain constant after ~2080, at a value about half of that at the end of the historical period (Clarke et al. 2007; Thomson et al. 2011). In the totally unmitigated scenario RCP8.5 (Riahi et al. 2007; Riahi et

330 al., 2011), rising emissions until the end of the century are assumed. The three scenarios impose a
maximum radiative forcing of 2.6, 4.5, and 8.5 W/m² compared to pre-industrial conditions.-

ERA-Interim reanalysis data

335 In addition to the climate simulation, we produced a hindcast run with RCA forced by ERA-Interim reanalysis
data at the lateral boundaries (RCA-ERA-Interim, Dee et al., 2011, Table 2). In this study, the hindcast was
compared with the original ERA-Interim data, which have a resolution of only 0.75° but the same temporal
resolution of 6 hours (Table 1). The original ERA-Interim data was interpolated onto the grid of the RCA
climate model. This comparison demonstrated the added value of downscaling. For a full description
of the ERA-Interim reanalysis data set, the reader is referred to Dee et al. (2011).

340 -

2.3 Detection of atmospheric rivers

~~We here employ the detection algorithm developed by Lavers et al. (2012) and Lavers and Villarini~~
~~(2013) which has been successfully applied both for hindcast simulations and climate studies (Lavers~~
345 ~~and Villarini, 2012; Lavers et al., 2013). First, the vertically Integrated atmospheric water Vapor~~
~~Transport (hereafter IVT) is calculated at every model output time step. The vertical integration is~~
~~done over the models pressure levels from 1000 to 300 hPa that were converted from the models~~
~~hybrid levels:~~

350 ~~Guan and Waliser (2015) described below and was performed for 30-year periods at the end of the~~
~~20th century (1970-1999) and at the end of the 21st century (2070-2099) i.e. for each of the RCP2.6,~~
~~RCP4.5, and RCP8.5 individually. Only the RCA-ERA-Interim hindcast run was done for 1979 to 2009.~~

355 ~~Atmospheric river detection can be basically done using their specific characteristics, namely the~~
~~extraordinary moisture transport and their elongated shape (width and length scales). A number of~~
~~studies addressed methods to detect ARs in model simulations and gridded reanalysis data (Lavers et~~
~~al., 2011; Lavers et al., 2012; Nayak et al., 2014; Nayak and Villarini, 2016; Gao et al., 2015; O'Brian~~
~~et al., 2020). An overview can be found in briefly~~
360 ~~The detection procedure of ARs is~~
~~A number of~~
~~studies have addressed methods to detect AR, based on model simulations in a Eulerian framework~~
~~(Lavers et al., 2011; Lavers et al., 2012; Nayak et al., 2014; Nayak and Villarini, 2016; Gao et al.,~~
~~2015; O'Brian et al., 2020). An overview of some of those methods can be found in Shields et al.~~
~~(2018). In our study, we employed the detection algorithm developed by Lavers et al. (2012) and~~
~~Lavers and Villarini (2013), as it has been successfully applied in hindcast simulations and in future~~
~~projections (Lavers and Villarini, 2012; Lavers et al., 2013). In this algorithm, vertically integrated~~
365 ~~atmospheric water vapor transport (hereafter IVT) is calculated at every 6-hourly model output time~~
~~step. The vertical integration is done over pressure levels ranging from 1000 to 300 hPa (Lavers et al.,~~
~~2012):~~

$$IVT = \sqrt{\left(\frac{1}{g} \int_{1000}^{300} q u dp\right)^2 + \left(\frac{1}{g} \int_{1000}^{300} q v dp\right)^2}$$

370 where g is gravitational acceleration [$m^3/(kg * s^2)$], q is specific humidity [kg/kg], u and v the are
horizontal wind components [m/s], and dp [Pa] is the pressure level difference of adjacent pressure

levels.

In the two hydrostatic models' hybrid level space, the IVT is balanced by precipitation minus evaporation.

375

Next, the detection algorithm is launched (Lavers and Villarini, 2013). It is composed of the following steps:

1. From the 6-hourly IVT time series between 1970-1999 all time steps at 12:00 UTC are extracted.

380

2. Along 10°W, all IVTs are sampled separately in seven meridional 5° bins between 35-70°N, i.e. 35-40°N, 40-45°N,... 65-70°N. Hence, the sample size for each meridional 5° bin consists of ~ 30 (years) * 365 (12:00 UTC) * N (number of grid cells in the respective 5°-bin at 10°W).

385

3. For each of the seven bins the 85th percentile IVT is calculated. The 85th percentile serves then as the threshold in the detection of AR (Lavers and Villarini 2012; Lavers and Villarini; Fig. 2).

After the bin specific IVT thresholds were determined, the entire IVT time series containing all time steps (00:00, 06:00, 12:00, 18:00) is searched for ARs.

390

4. AR are detected separately for each of the seven 5° latitudinal bins along 10°W and at every time step. If the max IVT within the respective bin exceeded the threshold for that bin (Fig. 2) a search is conducted from 10°W westward to 30°W and eastward to 25°E. All grid cells in which the threshold is exceeded are retained together with its time stamps (Lavers and Villarini, 2013).

395

5. The resulting AR time series is then further evaluated according to spatial and temporal criteria (Lavers and Villarini, 2013). Hence, the axis of a potential AR is determined as a maximum IVT value along subsequent longitudes and the total length is calculated. Following Lavers and Villarini, (2013) and Lavers et al., 2015), in our study only those fields in which the AR axis was longer than 1500 km were retained. Due to our limited domain, the algorithm does not detect AR that do not reach Europe but remain out over the Atlantic Ocean. Thus, across the western Iberian Peninsula, which is located relatively close to the model's western boundary, some AR might have been missed or detected with a delay (as it may take longer to reach the 1500-km criterion when the AR proceeds into the model). Over the UK and Norway, this did not have a significant effect as these countries lie far away from the model's lateral boundary.

400

405

6. At this stage the retained AR fields can contain more than one AR at every time step because an AR may cover two adjacent bins. These double entries are removed.

410

7. Finally, ARs are checked for "lifetime". ARs must have a lifetime of at least 18 hours, corresponding to three or more consecutive 6-hourly output time steps. All other time steps were discarded.

415

8. During the detection, for the purpose of post-analysis, AR masks are generated and archived at a resolution of 6-hourly time steps during the lifetime of the AR. The masks contain information on the moisture content as well as the date and time (Fig. 3). This allows calculation of the mean IVT within an AR. The masks are also used to calculate the mean precipitation associated with AR and to

analyze the routes taken by the AR over the European continent.

420

Then the 85th percentile IVT is calculated based on IVTs at 12:00 UTC time stamps and along 10°W longitude (Lavers and Villarini 2012; Lavers et al. 2013). Following Lavers et al. (2013) this procedure is done for meridional bins of 5° between 35–70°N. The resulting 85th percentile values served then as threshold for the detection of ARs (Fig. 2). After this pre-processing all 6-hour IVT fields are analyzed along 10°W and the 5° latitudinal bins at every single output time step. If the max IVT within an individual bin exceeded the threshold for that bin (Fig. 2) a westward and eastward search was done starting from 10°W to 30°W and 25°E. All grid cells where the threshold was exceeded were retained (Lavers and Villarini, 2013). Note: for the ERAI data set and the RCA-ERAI (Table 2) hindcast simulation the analysis period is 1979 – 2008, as ERAI data from before 1979 are not available.

425

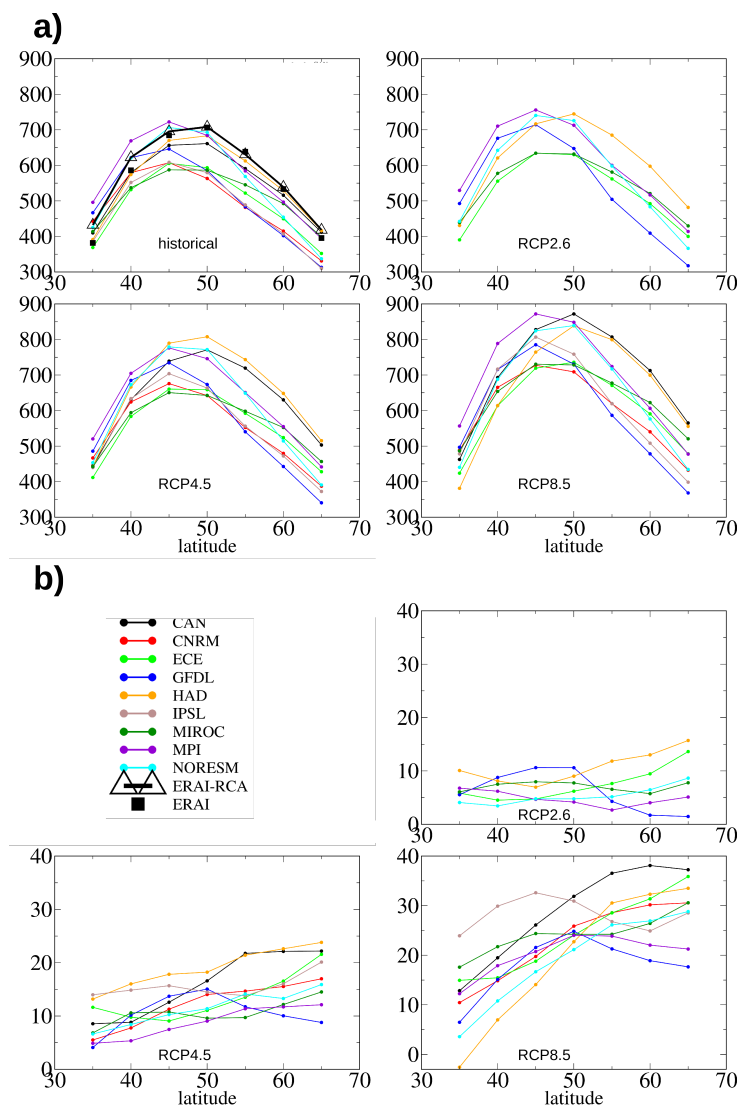


Figure 2: a) IVT 85th percentiles of IVT [$\text{kg m}^{-1} \text{s}^{-1}$] at 10°W [$\text{kg m}^{-1} \text{s}^{-1}$] thresholds for the ensembles' all models and the historical period (1970-1999, upper left) and the RCP climate scenarios (2070-2099) at 10°W used by the algorithm to track ARs. The algorithm uses the values to find AR. b) Relative change [%] in the IVT thresholds in future scenarios relative to the respective historical period.

430

Next, the resulting fields are further evaluated for spatial and temporal criteria (Lavers and Villarini, 2013). Hence the axis of a potential AR was determined as maximum along each longitude IVT of the structure. Only those fields were retained with an axis longer than 1500 km and then classified as AR. Furthermore, an AR has to be persistent over a period of at least 18 hours. Figure 3 shows a prominent example for an AR detected in the ERA-I reanalysis (left) and the ERA-I hindcast simulation (right) that demonstrably caused intense rain over Europe (Lavers and Villarini, 2013). The whole detection procedure is performed separately for the historical and future periods and for each of the ensemble members respectively provides an example of an AR that caused intense rain over France and Germany and was detected in the ERAI reanalysis (left) and in the ERAI hindcast simulation (right). The detection procedure is performed separately for the historical and future periods and for each model (Table 2).

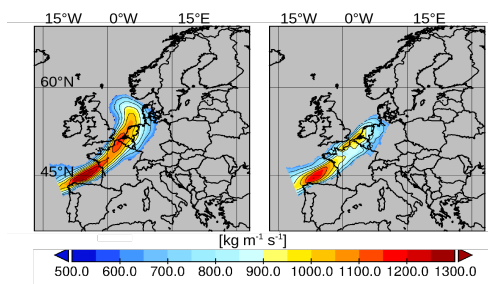


Figure 3: AR Atmospheric river associated with storm Lothar, detected in the ERA-I reanalysis (left) and in the ERA-I hindcast simulation (right), 25 December, 1999; 0:00:00 UTC. IVT values below the AR threshold 85th percentile are masked out.

2.4 Detection in future climate

Unlike previous studies (e.g., Lavers et al., 2013; Gao et al., 2016; Ramos et al., 2016), in this study we did not use the historical thresholds to detect ARs in a future climate. Instead, the IVT thresholds were calculated based on the respective climatologies between 2070 and 2099. This was done to keep the empirical relationship between the 85th percentile IVT and the moisture content in AR derived for the present climate. Hence, according to weather data for the years 1998–2005, the 85th percentile at noon (12:00) corresponded roughly to the median moisture content of the observed AR (see Lavers and Villarini, 2013 for details).

Figure 2 shows that the 85 percentile can strongly increase in the future climate depending on the scenario, the latitude, and the respective model. An example is RCA-CAN for which the IVT threshold increases by nearly 40% in RCP85 north of 55°N (Fig. 2b). In this simulation the 85th percentile IVT from the historical run at 55°N corresponds to the 68th percentile in the future period.

Hence, in this study a stable empirical relationship between the 85th percentile and the median was assumed. Consequently, our approach limits the influence of the larger mean atmospheric moisture content in the future climate and instead emphasizes dynamic changes.

2.5 Calculation of indices

465 The impact of AR under present and future climate was investigated by calculating the following indices:

470 1. **ARF**: The AR frequency expressed as a percent of AR days per total days within a 30-year period. A calendar day is classified as an AR day if within the 24 hours at least one AR event is recognized. Even if only one of the four 6-hourly time steps during the day is impacted by an AR, the day is counted as an AR day. Consequently, an AR lasting 18 hours and extending over two days is counted as two AR days.

475 2. **%AMP**: The percent annual maximum precipitation rate related to AR: For every land point, the maximum precipitation rate for every year is extracted together with the date and time of its occurrence. Then every grid cell is checked to determine whether this annual maximum is related to an AR at this time and position (using the aforementioned AR masks). Hence, if 15 out of the 30 annual maxima are attributable to AR, the %AMP is equal to 50%.

480 3. **%95P**: The fractional contribution (%) of AR-related precipitation to the total heavy precipitation (precipitation events > 95th percentile precipitation).

1) The precipitation is summed if the associated precipitation rate exceeds the 95th percentile precipitation calculated from all precipitation events.

2) This is repeated but only for those precipitation rates related to AR. Thus, the %95P is the percent contribution of AR-related heavy precipitation to the total heavy precipitation.

485 4. **%TP**: The same as the %95P but all precipitation events are considered. Thus, the %TP is the percent contribution of AR-related heavy precipitation to the total precipitation.

3. ARs in the historical climate historical simulations and hindcasts

490 3.1 Differences in IVT thresholds in historical, and hindcast simulations

A comparison of the latitudinal-dependent IVT thresholds of the RCA simulations with those derived from ERAI is shown in Figure 2a. As expected, the RCA-ERAI (triangles in Fig. 2a) hindcast simulation was closest to the ERAI reanalysis (filled squares). Notable discrepancies between the two data sets occurred at latitudes 40°N and 35°N. Due to the rotated grid of the RCA, the positions 35°N and 40°N at 10°W were closest to the western lateral boundary of the RCA (Fig. 1). The discrepancies most likely stem from known issues with lateral boundary coupling, as occurs in limited area models with one-way coupling to the global models (e.g., Davies, 2013; Chikhar and Gauthier 2017). Moreover, the southern model boundary at 35°N lies in the transition zone between dry air masses from the subtropics and the wet air masses of the westerlies. In this transition zone, large gradients in moisture content over short distances can be expected. Consequently, small differences in the mean position of the transition zone can cause large differences in the local moisture content.

The pronounced differences that characterize the different RCA historical simulations (Fig. 2a) reflect

505 the different climates derived from the parent global models at the lateral boundary. First, the parent
global models differ in their thermodynamic equilibrium states, such that both the air temperatures and
the moisture loads at the lateral boundary of the RCA differ as well. As a result, the large-scale
atmospheric circulation also differs among the global models (e.g., Brands, 2021), as the equator to
pole temperature gradients are likewise different (Harvey et al., 2014). This further influences the
meridional position of the westerlies in the respective models. For example, the maximum moisture
510 transports are located around 50°N in RCA-HAD, RCA-CAN, and RCA-MIROC but at 45°N in the
other historical runs.

There was no evidence of a linear relationship between climate warming and the and the increase in
IVT thresholds (Fig. 2b). For example, in RCA-HAD the IVT at 35°N in the low and moderate warming
scenarios (RCP2.6 and RCP4.5) increased by ~10% and ~15%, respectively (Fig. 2b). In the
strongest warming scenario (RCP8.5), however, the IVT decreased by ~5%. This suggests that, over
515 the long term, dynamic changes influence the IVT.

3.21 General statistics

Table 3 summarizes the and along 10°W) (expressed as total ARs detected in a 30-year period of
atmospheric rivers yfrequency for each run of the ensemble as well as from the ERAI reanalysis data
520 set and the hindcast run. The number of detected ARs in the RCA-ERAI hindcast (322) is nearly
identical with that analyzed from the ERAI reanalysis (321) itself which was used to drive the model.
This indicates that the number of ARs in RCA is primarily controlled by lateral boundary conditions
the. This is not surprising since ARs develop in open ocean regions far outside the model domain and
so the potential for alterations by the regional model is quite low. According to this, the number of
detectable ARs in the individual RCA historical climate simulations (Table 3) will likewise reflect the
525 ARs generated from the driving global climate model. Consequently, the RCA historical climate
ensemble exhibits a fairly large spread during the historical period ranging from 262 (RCA-MIROC) to
421 (RCA-NORESM). The difference between the ensemble mean of RCA historical simulations
(RCA-MEAN=359) and the RCA-ERAI hindcast run (n=322) is quite low compared to the standard
deviation over the RCA historical ensemble (58). summarizes the number of AR for each run of the
530 climate ensemble and the ERAI reanalysis data set and for the RCA-ERAI hindcast run. The results
were almost identical for the RCA-ERAI hindcast (322) and ERAI reanalysis itself (321), which was
used to drive the RCA. This indicates that the number of AR in the RCA is primarily controlled by the
parent global model at the lateral boundaries. This is not surprising since AR develop in open ocean
regions far outside the model's domain. However, within that domain the RCA develops freely, leaving
535 its own fingerprint on AR, by controlling their intensity, geometry, and lifetime. The RCA fingerprint is
likely to become stronger with growing distance from the lateral boundaries. Analogously, AR in the
respective RCA climate simulations (Table 3) will reflect the AR generated from the driving global
climate model. Consequently, the RCA historical climate ensemble had a fairly large spread during
the historical period, ranging from 262 (RCA-MIROC) to 421 (RCA-NORESM). The difference
540 between the ensemble mean (RCA-MEAN) of the historical simulations (RCA-MEAN=359) and the
RCA-ERAI hindcast run (n=322) was small compared to the standard deviation over the RCA
historical ensemble (58).

545

Compared to the historical period, RCA-MIROC increased by 15% in RCP 4.5 but only by 5% in the strongest warming scenario (RCP8.5, Table 3). Hence, there was no linear scaling with global mean warming. This can be explained by the changes in the large-scale circulation in the parent global model, such as induced by shifts in the eddy-driven jet (Gao et al., 2016).

550

	Historical/ Hindcast	RCP26	RCP45	RCP85
RCA-ERA1	322			
ERA1 reanalysis	321			
RCA-NEMO climate ensemble				
RCA-MEAN	359	390.0 (+8.6)	425.7 (+18.656)	445.6 (+24.1)
RCA-STD	58	67.4 (+16.46)	71.50 (+23.657)	90.3 (+56.0)
RCA-CAN	367		445 (+21.3)	447 (+21.8)
RCA-CNRM	285		317 (+11.2)	362 (+27.0)
RCA-ECE	393	396 (+0.76)	412 (+4.8)	468 (+19.1)
RCA-GFDL	351	367(+4.6)	388 (+10.5)	456 (+29.9)
RCA-HAD	397	422 (+11.3)	484 (+21.9)	565 (+42.3)
RCA-IPSL	409		498 (+21.8)	523 (+27.9)
RCA-MPI	304	311 (+2.3)	350 (+15.1)	392 (+29.0)
RCA-MIROC	262	264(+0.76)	302 (+15.3)	276 (+5.3)
RCA-NORESM	421	417(-0.91)	457 (+8.6)	521 (+23.8)

Table 3: Frequency expressed as nNumber of ARs detected in a 30 year period of different climate scenarios. The historical period is for all runs is 1970-1999. Only for the ERA1 runs it is 1979-2009. Numbers given in parenthesis denote relative change [%] in the future period compared to the historical period. The exception is the ERA1 run, for which it was 1979-2008. Numbers in parenthesis denote the relative change (%) in the future vs. the historical period.

Figure 4a compares the moisture transport by ARs over land which indicates the potential to force local heavy precipitation events. We note that the RCA-ERA1 run has a lower moisture content over land compared to ERA1 (-5%, Figure 4a). This is in line with the models cold bias in air temperature (Gröger et al., 2021a) which favors lower moisture contents. The probability distribution of diagnosed AR durations (Figure 4b) indicates no systematic differences between the ERA1 reanalysis, the hindcast run or the mean historical climate simulations. For all model realizations about half of the detected AR last for less than one day (Fig. 4). Noteworthy is the lower moisture content of nearly the entire RCA historical ensemble compared to the RCA-ERA1 hindcast simulation. Overall, this points to a systematic negative bias in moisture contents over land in the RCA model. A comparison of the moisture transported by AR over land is shown in Figure 4a, which depicts the potential of AR to force local heavy precipitation events. Note that the moisture content over land is lower in the RCA-ERA1 run than in the ERA1 (-5%, Fig. 4a). This is in line with the model's cold bias in air temperature (Gröger et al., 2021a), thus favoring a lower moisture content. The lower moisture content in RCA-

555

560

565 MEAN than in the RCA-ERA1 hindcast simulation should also be pointed out. Overall, this suggests a
 systematic negative bias in the moisture content over land in the RCA model. The distribution of
 diagnosed AR durations (Fig. 4b) does not indicate systematic differences between the ERA1
 reanalysis, the hindcast run, and the mean historical climate simulations. For all model realizations,
 about half of the detected AR lasted one day or less (Fig. 4b)

570

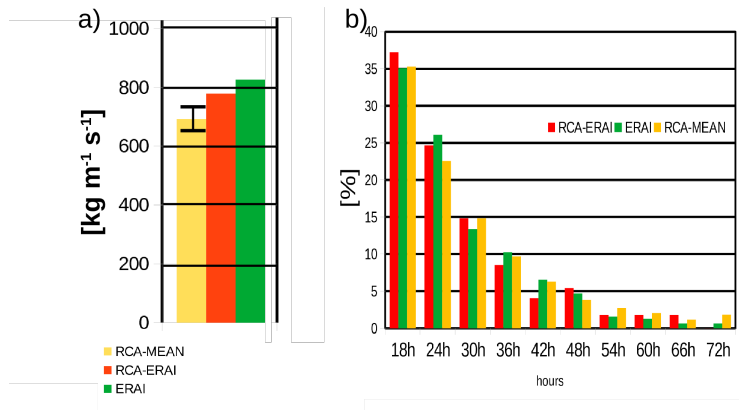


Figure 4: a) Average AR moisture transport over land-by-ARs for each model realization depicted from the climatological historical period (RCA-MEAN) as well as for the hindcast simulation (RCA-ERA1) and the reanalysis data set (ERA1). For RCA-MEAN the range of two standard deviations from individual realizations model simulation is given. b): Histogram of average durations of detected ARs.

3.23 Impact on precipitation

575 In a first step we estimate the likelihood for a certain region to be affected by an AR. As a simple
 index, we count the total number of days Error: Reference source not found) during which a
 land cell was covered by an AR (AR days, . As expected, ARs are most present over the UK and the
 coastal regions of western Europe. Further inland the AR imprint declines as ARs lose moisture due
 580 to rainfall and thus do not further meet the IVT threshold (Fig. 2). Strong moisture loss is also
 indicated along the Norwegian coast where the landfall of ARs cause strong rain events due to
 uplift. Maps of AR frequencies (ARF) over land are presented in Figure 5a. As expected, during the
 historical period AR were most abundant over the UK and the coastal regions of western Europe.
 Further inland, AR frequencies declined as the AR lost moisture due to rainfall and thus no longer met
 the IVT threshold (Fig. 2). Strong moisture losses also occurred along the Norwegian coast, where AR
 585 landfalls caused heavy rain events due to orographic uplift.

Next we quantitatively evaluate t of yearly maximum of daily precipitation that is caused by
 ARs portion the imprint of ARs on extreme precipitation by calculating the . The result is shown in Fig.
 590 Error: Reference source not foundb which shows the percentage of yearly maximum daily
 precipitation rates forced by ARs. ARs explain up to ~60% of the yearly maxima precipitation rates
 over southwestern Norway. A strong imprint is likewise seen over western UK and along the
 European coasts. We then evaluated the potential of AR to cause annual maxima of daily precipitation
 (Fig. 5b, %AMP). Locally, AR explained up to ~60% of the yearly maxima over southwestern Norway.
 595 A strong imprint was likewise seen over the western UK and along European coasts, where AR were

| responsible for up to 50% of the annual maxima in RCA-MEAN and RCA-ERA1.

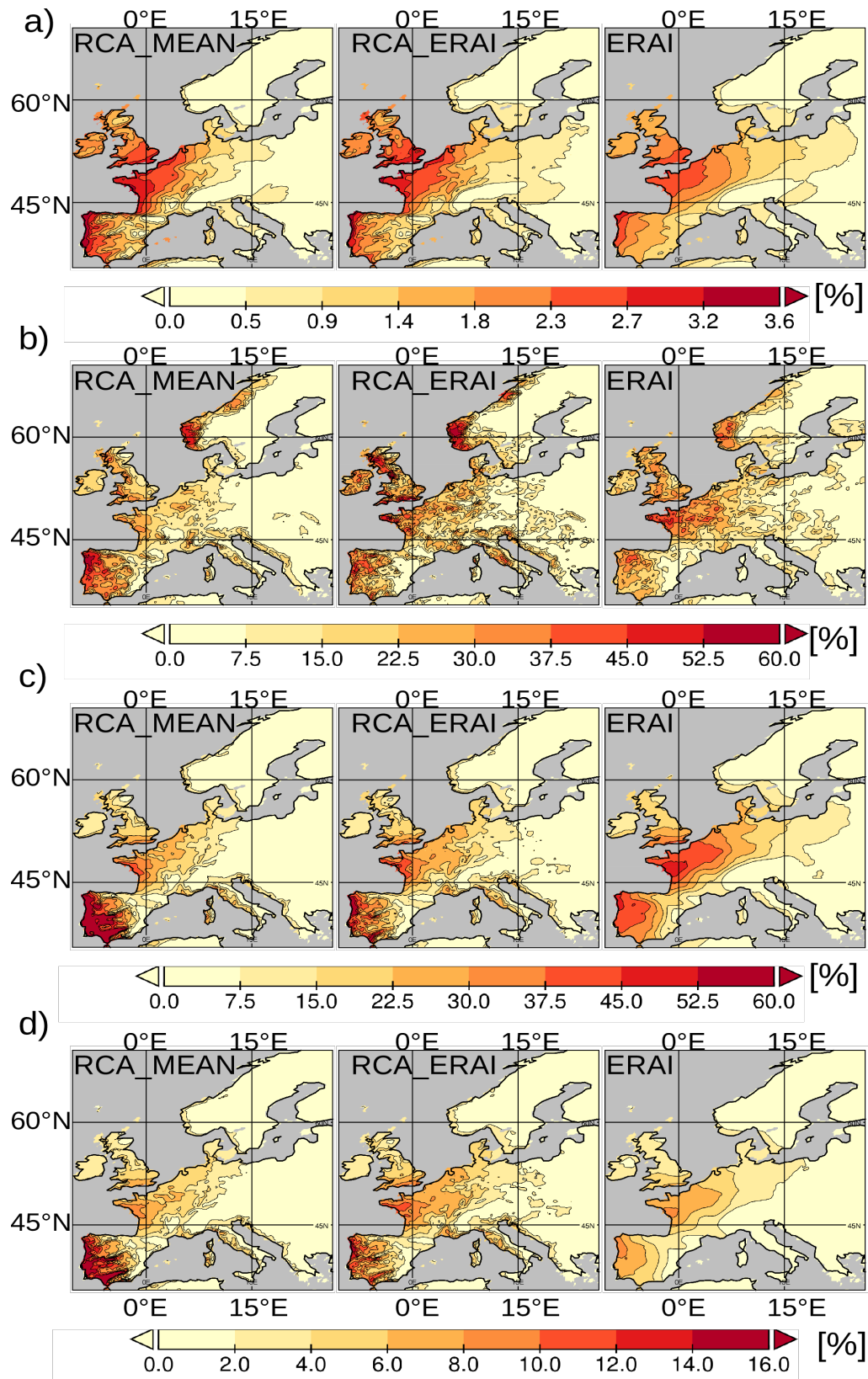


Figure 5: AR frequency expressed as the total number of days a grid cell was covered by an AR during the historical period (ARF). b) Percentage of the annual maximum precipitation related to AR (%AMP). c) Fractional contribution of AR-forced precipitation to the >95th percentile precipitation (%95P). d) Same as c) but for the total precipitation (%TP).

600

605

610

615

Besides their potential to cause yearly precipitation maxima, AR give rise to heavy precipitation events. The fractional contributions of AR to heavy precipitation (%95P) and to the total precipitation (%TP) are shown in Figure 5c and 5d. The spatial pattern mainly mirrored the AR frequency pattern but it also reflected the varying long-term mean hydrological conditions in Europe: In semi-arid regions such as the Iberian Peninsula and along the western coast of Italy, %95P increased to almost 60% and 30%, respectively. Under the humid climate of central and western Europe, the %95P was smaller but it reached 40% in western France and the southern UK (Fig. 5c). In the mountainous regions of Norway and in the Alps, i.e., regions with very high mean precipitation and frequent convective rain events, the influence of sporadic AR was accordingly low. A similar pattern characterized the fractional contribution to the total annual precipitation (%TP, Fig. 5d). Maxima occurred over western France and the western Iberian Peninsula, where AR accounted for up to 10% of the total precipitation.

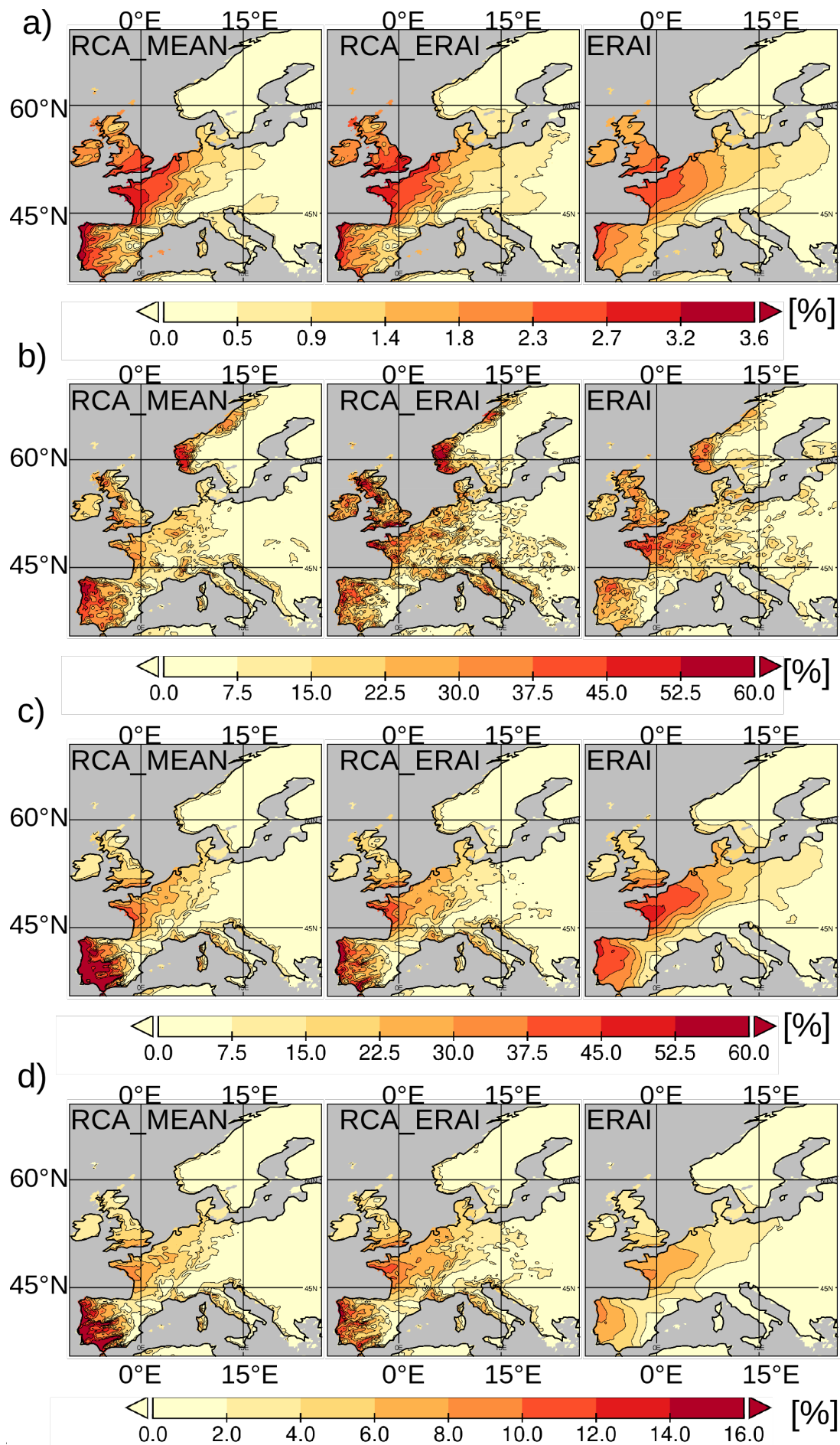


Figure 6: a) AR frequency expressed as total number of days a grid cell was covered by an AR during the historical period (ARF). b) Percentage of annual maximum precipitation related to ARs (%AMP). c) fractional contribution of AR forced precipitation to the >95th percentile precipitation (%95P). d) same as c) but for the total precipitation (%TP)

620 Besides their potential to force yearly precipitation maxima ARs strongly affect the fraction of heavy precipitation events. Here we investigate the AR contribution of precipitation to the total annual precipitation (Figure Error: Reference source not foundd) and to the fraction of heavy precipitation (Figure Error: Reference source not foundc). The spatial pattern mainly resembles the pattern seen in the AR days (Figure Error: Reference source not founda) but further reflects the mean climatic conditions in Europe. These are also the regions which are frequently affected by ARs (Fig. Error: Reference source not founda). precipitation to the >95th percentile (Bretagne) contributes up to 40% related rain AR. In humid regions of central and western Europe, in semi-arid regions like the Iberian Peninsula the contribution increases to almost 60% which compares well with results from gridded reanalysis data sets (Lavers and Villarini, 2015) although ARs do not notably cause annual maximum precipitation rates (Fig. Error: Reference source not foundb). (Fig. Error: Reference source not foundd). A considerable contribution is likewise seen along the western coast of Italy. Here AR contribution is up to 30%. In the topographically elevated regions of Norway and over the Alps, i.e. regions supporting often strong convective rain events, the influence of ARs is also less pronounced. As expected in more humid regions of eastern Europe and Scandinavia ARs contribute only minor amounts to the annual total. A similar pattern is shown for the contribution to the total annual precipitation (Figure Error: Reference source not foundd). Maxima contributions are seen over western France and the western Iberian Peninsula where ARs contribute up to 10% to the total precipitation.

3.4 Effect of Downscaling

640 The effect of downscaling was assessed by comparing the 0.75° ERAI reanalysis (Fig. 5, right column) with the 0.22° RCA-ERAI hindcast simulation (Fig. 5 middle column). The lower resolution of ERAI eliminated much of the spatial variability, thus highlighting the effect of the downscaling by RCA. This was most visible in the noisy precipitation-related indices %AMP, %95P, and %TP (Fig. 5b–d). This was expected because spatial precipitation patterns are modulated by stochastic processes associated with, e.g., small convection cells and further affected by topography. The representation of convection cells and topography has been shown to benefit from a higher resolution (e.g., Feser et al., 2011; Hoheneger et al., 2020; Stevens et al., 2020). The pronounced effect of a higher topographic resolution was seen over the Iberian Peninsula. Here, RCA-ERAI clearly resolved the distinct effect of the prominent west–east topographic features seen in the fractional contributions to the precipitation budget. Those features appeared as small distinct WSW-ENE bands of alternating high and low %95P and a %TP that followed the topographic elements built up by the Sistema Central Plateau, the Sierra Morena mountains, and the Penibaetic orogenic system (Fig. 5c,d, and middle columns). By contrast, in ERAI (Fig. 5c,d, right column) there was a simple decline of the %95P while the %TP occurred at a longer distance from the coast and did not reflect any topographic imprint. For the Iberian Peninsula, added value of regional downscaling was previously reported for the simulation of mean precipitation and mean temperature patterns (Gomez-Navarro et al., 2011).

660 Another noteworthy difference was the considerably larger number of AR-related annual maxima (%AMP, Fig. 5b) over Norway, West Scotland, and Italy in RCA-ERAI than in ERAI. In the latter, the AR influence on %95P and %TP was much more extensive in eastern Europe. However, there are no major topographical elevations in eastern Europe, which suggests that resolution is not the only factor accounting for this difference. Rather, differences in the model's physics (e.g. cloud

665 formation) and the surface boundary conditions (e.g., surface temperature, surface roughness parametrization) between RCA-ERA1 and ERA1 could influence the extent of AR penetration into eastern Europe.

670 Finally, we note that the comparison between different spatial resolutions might also reflect different noise levels. This noise occurs when isolated grid points located outside the AR at a given time step exceed the IVT threshold but do not satisfy the geometric and temporal requirements. The different noise levels would then contribute to the total effect of downscaling.

675 3.5-2.2 Comparison of the RCA ensemble mean with the ERA1 hindcast and ERA1 reanalysis

In the historical simulations, i.e. when the model is forced by climate output the regional coupled models develop their own weather regimes which can not be expected to be in phase with recorded weather data. Therefore, individual AR incidences can be analyzed only statistically which is done in terms of calculated indices during the climatological historical period (Fig. Error: Reference source not found).

685 We now compare the results of the RCA historical ensemble mean (Figure Error: Reference source not found, left column) with the RCA-ERA1 hindcast (Figure Error: Reference source not found, middle column) and the ERA1 reanalysis data (Figure right column) in which internal natural variability can be expected to reflect the observed weather. Global climate models can have considerable biases on a regional scale. Consequently, when driven by global climate models at the boundaries, RCA will not perform as well as hindcast models when the driving lateral boundaries are constrained to reanalysis data. Therefore, in the following, before assessing climate change scenarios, we briefly compare the results of the RCA historical ensemble mean (RCA-MEAN, Fig. 5, left column) with the RCA-ERA1 hindcast (Fig. 5, middle column) and ERA1 reanalysis data (Fig. 5, right column).

695 Figure Error: Reference source not found demonstrates that for most of the above described indices the RCA historical ensemble mean represents reasonably well the spatial pattern found in the RCA-ERA1 simulation. The spatial correlation coefficients between RCA-ERA1 and RCA-ENSM are respectively calculated as 0.98 for AR the frequency (Fig. Error: Reference source not founda), 0.82 for the percentage of yearly maximum precipitation (Fig. Error: Reference source not foundb), and respectively 0.92 for contribution to total annual and heavy rain precipitation amount (Fig. Error: Reference source not foundc,d). For ARF, %AMP, %95P, and %TP, RCA-MEAN reasonably well reproduced the spatial pattern obtained with the RCA-ERA1 simulation. The spatial correlation coefficients between RCA-ERA1 and RCA-ENSM were 0.98 for ARF (Fig. 5a), 0.86 for %AMP, 0.82 for %TP (Fig. 5b), and 0.92 for %95P (Fig. 5c,d). Similar to RCA-ERA1, the imprint over eastern Europe was distinctly weaker according to RCA-MEAN than according to the ERA1 data set.

705 Pronounced differences between RCA-MEAN and RCA-ERA1 also occurs over the Iberian

710 Peninsula, where the values of %AMP, %95P, and %TP are systematically higher in RCA-MEAN. Overall, the best match between RCA-MEAN and RCA-ERA1 is for the parameter ARF (Fig 5a). As ARF is calculated only from the IVT, it is less effected by biases in precipitation. Thus, the main contributor to the biases of RCA-MEAN seen in %AMP, %95P, and %TP are attributable to the simulated precipitation, not to the IVT.

715 Besides the spatial pattern seen in the AR indices, the detected ARs also undergo a strong seasonal cycle. Figure Error: Reference source not found shows that ARs are most abundant during fall and early winter. A pronounced difference is, however, seen in August where the relative share is about twice as much in the RCA historical ensemble compared to the ERA1 hindcast which implies that the AR season starts a bit too early in the RCA ensemble. However, all in all we find that spatial patterns and the seasonal cycle of ARs is well preserved in the models climate mode compared to the ERA1 data set and the ERA1 hindcast. The detected AR were also characterized by a strong seasonal cycle that was well reproduced by RCA-MEAN. Figure 6 shows that AR were most abundant during fall and early winter. The only notable difference was in August, when the relative share was about twice as large in the RCA historical ensemble than in the ERA1 hindcast. However, overall, AR were better represented in the model's climate mode (RCA-MEAN) than in the RCA-ERA1 hindcast simulation.

725

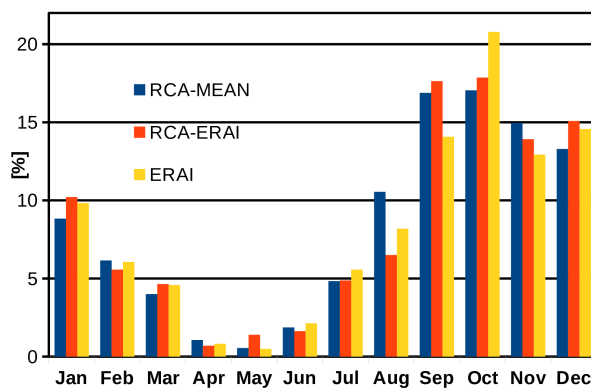


Figure 7: Seasonal cycle of detected AR at 10°W, expressed as the percent share of the total number of detected AR. The reference period for the RCA historical ensemble (RCA-MEAN, blue) was 1970–1999 and for the ERA1 hindcast (orange) and ERA1 (yellow) reanalysis 1979–2008. Seasonal cycle of detected ARs expressed as percentage share of total number of detected AR. The reference period for the RCA historical ensemble (blue) is 1970–1999 and for the ERA1 hindcast (orange) and ERA1 (yellow) reanalysis it is 1979–2009

3.2.3 Effect of regionalization

The above described spatial characteristics is also well reflected in the ERA1 reanalysis data (Fig.

735 Error: Reference source not found, left column). However, the lower spatial resolution of this data-
set (approx. factor of 10, Table 1) destroys much of spatial variation which demonstrates the effect
of the downscaling by RCA. This is more visible in the precipitation-related indices (Fig. Error:
740 Reference source not foundb-d) than in the AR frequencies (Fig. Error: Reference source not
founda). This is expected as precipitation patterns are modulated by stochastic processes and
further modulated by topography while the integrated atmospheric moisture transports (used to
detect and track ARs) are less affected by small-scale patterns.

(2021a) showed that RCA has a negative temperature bias against the observational E-OBS data
set. This means that air masses enter the lateral model boundary with a thermodynamically too
high moisture load. The adaption, i.e. the loss of moisture when the air masses are confronted
745 which the mean thermodynamics state of the inner RCA domain, probably takes longer for fast
moving air masses like within ARs. This would favor the detection of too many ARs., Gröger et al.

Another slight but noteworthy RCA-ERA5 vs ERA5 difference is seen in the seasonal distribution of
ARs. In the RCA-ERA5 hindcast the fall maximum is already registered in September while in ERA5
750 it is recorded for October. The most likely explanation for this is a temperature bias introduced by
RCA.%. Here, the lower resolution likely smooths heavy precipitation events. Furthermore, the
local maxima of AR contributions seen along Italy are by far less pronounced in the coarser ERA5
reanalysis (Fig. Error: Reference source not foundc,d). Apart from this, we also find a notably lower
amount of annual precipitation maxima related to ARs (Fig. Error: Reference source not foundb).

755 Over Norway the difference can be as large as 15 following the topographic elements build up by
the Sistema Central Plateau, the Sierra Morena mountains, and the Penibaetic orogenic system
(Fig. Error: Reference source not foundc,d). AR precipitation Apart from this, the downscaling effect
is most pronounced in regions with elevated topography as well as in in semi-arid climate zones of
southern Europe. Over Iberia the RCA-ERA5 run clearly resolves the distinct effect the of the west –

760 east striking topographic features seen in the contributions to the precipitation budgets. They occur
as small WSW-ENE striking bands of alternating high and lower hindcast run. This implies ARs
tend to penetrate less far inland after landfalling in the downscaled run. ERA-5 In turn, AR-
frequencies in the distal parts of eastern Europe are higher in the reanalysis data than in the (Fig.
Error: Reference source not founda,c,d). data set original ERA5 thenotably higher AR frequencies
765 and larger contribution to the total precipitation (and >95th percentile precipitation) along the coasts
compared to RCA-ERA5 run shows the downscaled

The added value of regionalization is demonstrated by the comparison between the high resolution
RCA-ERA5 run with a resolution of 0.22° and the corresponding ERA5 data set with a resolution of
0.75°. First,

770 Finally, we note that the global CMIP5 models used to drive RCA have an even lower resolution
ranging between 1.4° (CNRM) and 3° (CAN) which is notably lower than the ERA5 reanalysis data
set. This implies that the added value of regionalization in the future scenarios can be expected of
even greater importance.

775 4. Future climate change impact on ARs

4.1 General response of AR frequency and frequency and intensity

Figure 8 summarizes the relative change in average moisture transport by ARs according to the different greenhouse gas scenarios and for each of the downscaled global models. Consistently, ARs become more intense i.e. they have a higher moisture load in a warmer climate. The intensity at the end of the century increases on average by 9% (RCP2.6), 13% (RCP4.5), and 24% (RCP8.5) which is more or less in line with the corresponding increases of IVT thresholds (Fig. 2). The relative change in average moisture transported by AR for each of the GHG emission scenarios and each of the downscaled global models is summarized in Figure 7. AR became consistently more intense, i.e., they had a higher moisture load, in a warmer climate. The average intensity at the end of the century indicated by RCA-MEAN increased by 6% (RCP2.6), 13% (RCP4.5), and 24% (RCP8.5). These values are generally in line with the corresponding increases in the IVT thresholds (Fig. 2b).

Besides intensity, also the frequencies of detected ARs increases (RCP2.6=8.6%; RCP4.5=18.6%; RCP8.5=24.1%; Table 3) which are roughly proportional to the increase in intensity. However, not only the frequency of ARs increases but also the spread of the individual realizations at the end of the century. The relative change in ensemble spread (Table 3, 2nd row) increases even more than the ensemble average (RCP2.6=16.5%, RCP4.5=23.6%, RCP8.5=56.0%). This highlights the large uncertainty with respect to the chosen global model used for downscaling. Some advanced approaches for weighted model averaging were developed to reduce this type of uncertainties and have been tested for the case of AR over the US (Massoud et al., 2019; Massoud et al., 2020; Wootten et al., 2020). The number of detected AR also increased (Table 3). For RCA-MEAN, this number increased by 9%, 19%, and 24% in RCP2.6, RCP4.5, and RCP8.5, respectively. These values were roughly proportional to the increase in intensity. However, not only the frequency of AR but also the spread of the individual realizations at the end of the century increased. The relative change in the ensemble spread (Table 3, 2nd row) increased even more than the ensemble average (RCP2.6=17%, RCP4.5=24%, RCP8.5=56%). This highlighted the large uncertainty with respect to the chosen global model used for downscaling. Advanced approaches for weighted model averaging have been developed to reduce this type of uncertainty and have been tested for AR occurring over the US (Massoud et al., 2019; Massoud et al., 2020, Wootten et al., 2020).

-

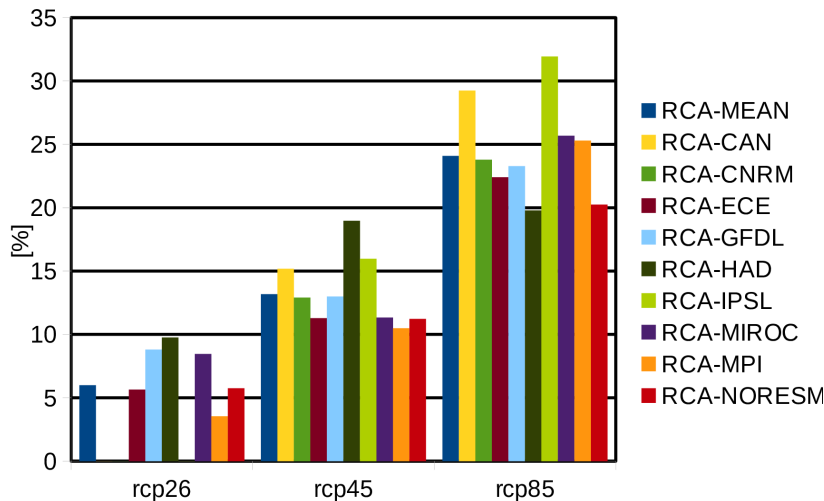


Figure 8: Relative change in moisture transport within ARs at the end of the century (2070-2099) compared to the historical period (1970-1999). *RCA-MEAN* denotes the mean of the individual models. Note no realization are available for *RCA-IPSL*, *RCA-CAN*, and *RCA-CNRM*.

4.2 Spatial changes

815 Next we analyze spatial pattern changes in future AR imprint demonstrates Figure 9a First, AR frequencies are addressed. an overall increase in the frequency of AR days is strongest which in over the southwestern sector of the Atlantic (Biscay) and adjacent land areas with maximum response over western France and the southern UK. This pattern is more or less consistent across the RCP scenarios but differs in strengths ranging from +20% to more than 200% (Fig. 9a) The change in the spatial patterns is shown in Fig. 8. An overall increase in AR day frequency was determined for scenarios RCP4.5 and RCP8.5 (Fig. 8a). The strongest increase occurred near the Bay of Biscay and adjacent land areas (western France and southern UK). This response over land was more or less consistent across the RCP scenarios but differed in strength, ranging from +0.2% to > +1.8% in RCP4.5 and RCP8.5 (Fig. 8a). This corresponds to a relative increase of 20–120% (RCP4.5) or 40–250% (RCP8.5) over Iberia, the UK, France Germany, and along the Norwegian coast.

825 In a first step the impact on the AR forced yearly maximum precipitation is addressed (Fig. 9b) patterns

830 We now investigate how the increased AR frequencies influence precipitation The most robust change is the strong increase over the western-central part of Europe which extends from western France along the coast of Belgium, the Netherlands northern Germany and Denmark up to the southern coast of Norway. Further spots of stronger AR impact are also visible along the northwestern tip of the Iberian Peninsula and the southern part of the UK. This general response is by far strongest in the unmitigated RCP8.5 scenario. In the moderate scenario RCP4.5 the changes are less pronounced in eastern-central Europe (Germany, Denmark). In the mitigation scenario RCP2.6 notable robust changes are restricted to a small area in NW France (Bretagne, Normandy). detected no robust changes are Fig. Error: Reference source not found b) see (during the historical period values are found highest there) Over southern Scandinavia Next we

840 address the number of AR forced heavy precipitation events. Figure 9c shows the number of
events nearly everywhere increases. The strongest response is seen over southern Scandinavia
where the relative increases exceed 300%. Over the western European continent and the UK the
average increases are in the range between 75-150% pointing to a roughly doubling risk for
flooding. Apart from this very strong increases (>300%) are noticed over eastern Europe (Figure
9c). Although in this region absolute AR occurrences are rather low, the strong relative increases
845 indicate a further eastward propagation of AR under the warmer future climate compare to present
day.

850 Figure 8b shows the changes in the yearly maximum precipitation attributed to AR (%AMP). The
most robust change was the strong increase over the western central part of Europe, extending
from western France along the coast of Belgium, the Netherlands, northern Germany, and
Denmark up to the southern coast of Norway. Further sites of stronger AR impact were also visible
along the northwestern area of the Iberian Peninsula and the southern UK whereas over southern
Scandinavia there were no robust changes. However, in this area %AMP was already very high
during the historical period (Fig. 5b), which limited the potential for further increases. This increase
over the UK, France, western Germany, and Iberia was by far the strongest in the unmitigated
855 RCP8.5 scenario. In the moderate scenario RCP4.5, the changes were less pronounced in eastern
central Europe (Germany, Denmark). In the mitigation scenario RCP2.6, robust changes were
restricted to a small area in NW France (Brittany, Normandy).

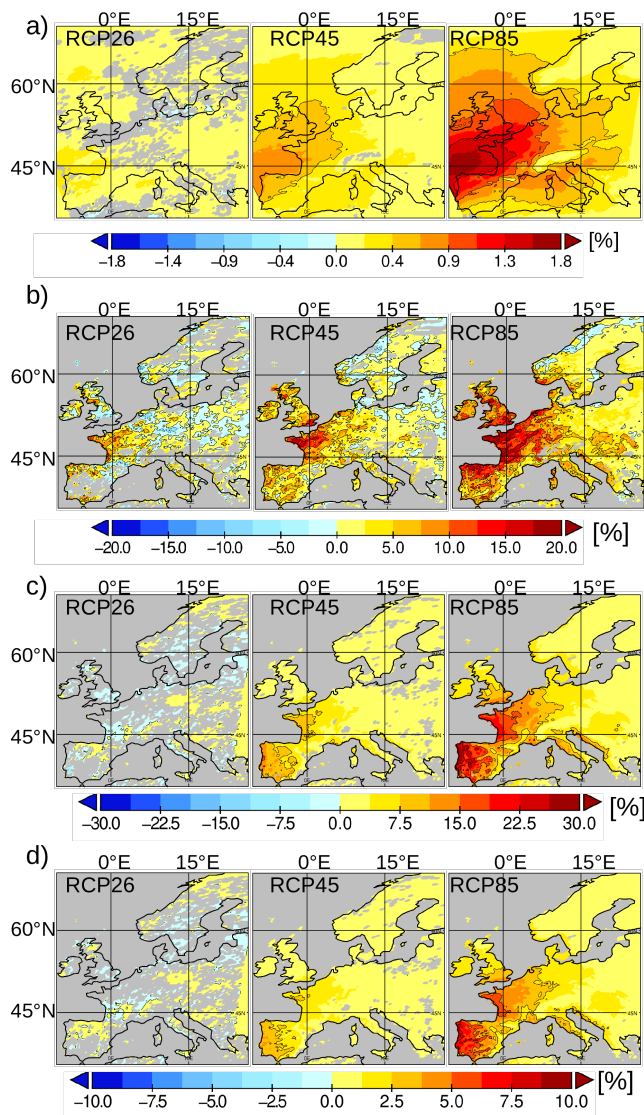


Figure 9: Difference between 2070-2099 minus 1970-1999 climatological indices for the RGA ensemble (i.e. the % values for the future minus the % values for the historical). a) AR days frequency (ARF). b) AR forced yearly maximum precipitation rates (%AMP). c) Number of AR forced rain events within >95th percentile fraction. d) Change in the contribution of AR forced precipitation to the heavy rain precipitation fraction (>95th percentile precipitation total %95P). e) same as c) but for the contribution fraction to the annual total precipitation (%TP). Note that all non-robust changes (at least 66% of downscaled runs agree on the sign of change) have been masked out. ~~shown~~ are land changes over only For b)–e).

865

The higher AR frequencies and moisture loads have also consequences for the local precipitation budget. Figures 9 displays the changes in the contribution of ARs to the heavy precipitation fraction (Fig. 9d) and the total annual precipitation (Fig. 9e). Most pronounced changes are seen in regions where already under historical climate condition contributions large are seen (Fig. Error: Reference source not foundc,d). Strongest increases are primarily seen over Iberia with changes up to +30% to the heavy rain precipitation and up to 20% along the French coast (Bay of Biscay) compared to the

870 historical period. The higher AR frequencies and moisture loads also had consequences for local
precipitation budgets. The fractional contributions of AR to the heavy precipitation fraction (%95P, Fig. 8c) and to the total annual precipitation (%TP, Fig. 8d) increased nearly everywhere. The most pronounced changes were in regions where the %95P and %TP were already large under historical conditions (Fig. 5c,d). In RCP8.5, the strongest increases primarily occurred in western Iberia and along the French coast (Bay of Biscay), where heavy rain precipitation increased by up to +30% and up to 20%, respectively, compared to the historical period

880 t least for the moderate and high greenhouse gas scenarios RCP4.5 and RCP8.5 the contribution-anomalies are robustly positive (Fig. 9d,e). The positive anomalies imply that in these regions the AR-induced precipitation rates increase stronger than mean precipitation rates.
response of different The mean precipitation and AR induced precipitation depicted in Figure 10 illustrate climate change. The climatological mean change (Figure 10a) shows the typical change in precipitation over Europe pointing to dryer conditions over southern Europe and wetter conditions over northern Europe (e.g. Jacobs et al., 2014; Kjellström et al., 2018; Teichmann et al., 2018; Gröger et al., 2020a; Christensen et al., 2021). Hence, mean precipitation rates increase only slightly by up to maximal 12 % over central Europe or even decrease over southern Europe. By contrast, AR induced precipitation increases between -25 - 40% over central Europe (Fig. 10b). In fact AR induced precipitation ranges are in most regions equally high as mean winter precipitation changes (not shown), i.e. the season where mean changes are highest. Decreasing AR precipitation is found in southern Europe but the reductions are less strong compared to mean rates. The only exception is Norway where in fact AR induced precipitation decreases while mean rates increase. This likewise explains the low response of annual maximum changes (Fig. 9b). The elevated AR fractional contributions %95P and %TP in RCP4.5 and RCP8.5 (Fig. 8c,d) suggested that in these scenarios the increase in the AR induced precipitation rates was higher than the increase in the average precipitation rates.

895 The changes in mean precipitation and AR-induced precipitation for RCP8.5 are compared in Fig. 9. The mean precipitation change (Fig. 9a) was consistent with the typically dryer conditions over southern Europe and the typically wetter conditions over northern Europe (e.g. Jacobs et al., 2014; Kjellström et al., 2018; Teichmann et al., 2018; Gröger et al., 2021a; Christensen et al., 2021). Hence, mean precipitation rates increased only slightly, by at most 12%, over central Europe or even decreased over southern Europe. By contrast, AR-induced precipitation increased -25-40% over central Europe (Fig. 9b). Decreasing AR precipitation also occurred in southern Europe but the reductions were weaker than the reductions in the mean rates. The exception was Norway, where AR-induced precipitation decreased while the mean rates increased. The lower AR precipitation rates well agree with the low response in western Norway of the %AMP, which locally even decreased (Fig. 8b).

910

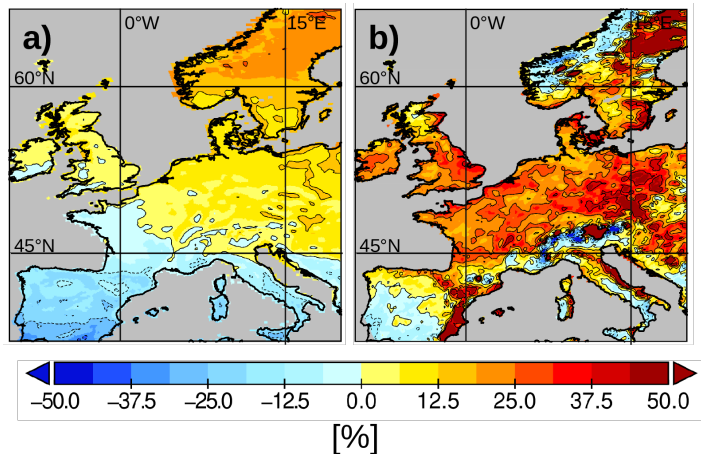


Figure 10: a) Relative change (difference between 2070-2099 and 1970-1999) in a) the average precipitation rates and b) the AR induced precipitation rates for RCP8.5. Relative change in mean precipitation rates for RCP8.5. b) Relative change in AR-induced precipitation rates.

4.3 Influence of potential dynamical changes

In the mid to high latitudes it has been found, that climate changes in mean and extreme precipitation takes place at similar magnitudes and mainly reflect thermodynamical processes (i.e. increasing water carrying capacity with warming air, e.g. Emori and Brown, 2005). Exceptions from this occur only when large scale circulation changes with further impact on moisture transport are involved (Emori and Brown, 2005). The dynamic changes were investigated by exploring the route followed by AR east of the 10°W meridian. In this analysis, AR masks were used (see Fig. 3) and, for the model's land grid cells the corresponding latitudinal position where the AR crosses the 10°W meridian was determined. All land grid cells overlain by the respective AR were then flagged with the latitudinal bin at 10°W (for example, 45°N for the bin 45-50°N). The flagged masks were then used to calculate, for every land cell, the percent share for every latitudinal bin (with the sum of all bins at every land point defined as 100%). This was done for the periods 1970-1999 and 2070-2099. Then, the future change (difference between 2070-2099 and 1970-1999) was calculated for RCP8.5. Finally, the latitudinal bins were consolidated into three main meridional bands: south of 45°N, 45-60°N, and north of 60°N. Based on global CMIP5 models Gao et al. (2016) suggest that thermodynamics is also the main driver AR related precipitation changes but may be modulated by dynamical circulation changes due to changes in the Jet position.

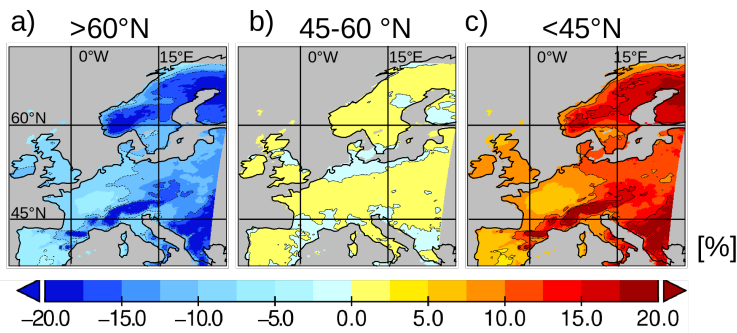


Figure 11: Analysis of AR origin in the RCA ensemble. Change in the origin of AR events related to latitudinal bands at 10°W. a) Relative contribution of regional AR occurrences originating from the Atlantic north of 60°N. b) 45-60°N, and c) south of 45°N same as a but for ARs originating from south of 45°N. The change (difference between 2070 – 2099 and 1970–1999) for RCP8.5 is shown. Shown is the change for RCP8.5 (2070–2099 minus 1970–1999).

930 In order to investigate potential dynamical changes we now elaborate more about the pathway of ARs
 on their way from the open ocean to the continent. It is not feasible to analyze the movement of
 every single AR over time. Instead, we here perform a simple analysis to determine the AR source
 region for every AR. Hence we check for every AR incident registered on land at which latitude the AR
 entered the European sector along 10°W meridian. We here consider the latitudinal bins south of
 935 45°N, 45–60°N, and north of 60°N. From this statistic we calculated for every land cell the percentage
 share of AR incidents for every latitudinal band (so that the sum of all bins at every land point sums up
 to 100%). The analysis is done for high emission greenhouse gas scenario RCP8.5 compared to the
 historical period.

940)-b°N (Fig. 11b) of north°N (Fig. 11a) and 45– of south for the latitudes contributions shows the change
 in the relative Figure 11 Overall, the RCA ensemble clearly shows a relative increase of those ARs
 originating south of 45°N degree (Fig. 11a). Most prominent increases are seen over the Alpine
 region and Scandinavia whereas western and central Europe are less affected. Between 45 and 60
 945 °N the changes are everywhere below 5% (not shown) indicating a more or less unchanged
 contribution within this latitudinal band.

By contrast, AR contributions from >60°N are diminished (Fig. 11b). Over Scandinavia ARs from
 >60°N contribute around 70–90% to the total AR events during the historical period (not shown). This
 contribution is reduced by ~20% in RCP8.5 (Fig. 11b) Our analysis showed not only the more frequent
 950 occurrence of AR in the future at all latitudes but also a change in their composition (with respect to
 the meridional band where they originate). AR contributions from >60°N declined everywhere (Fig.
 10a), with a ~20% reduction over Norway (Fig. 10a). The smaller fraction was paralleled by a relative
 increase in AR originating from south of 45°N (Fig. 10c) while the fraction from 45°–60°N was more or
 less unchanged (Fig. 10b).

955 and thus likely explains the aforementioned decreased AR precipitation rates (Fig. 10b).

In summary, we can conclude that ARs from the southern Atlantic sectors are more present over most

960 land regions in a warmer climate. By contrast, ARs arriving from the northern sectors of the Atlantic
are relative diminished over land (Fig. 11b).— transported over a longer distance across the central
continent compared to those ARs originating from >60°N. has to beIn turn, this shift suggests that the
moisture — that cross Scandinavia of ARsoriginHence, for Scandinavia this implies a profound
southward shift in the—The larger fraction of more southern ARs over Norway (and the smaller fraction
965 from >60°N) has two implications: 1) the more southern AR will carry warmer air masses to
Scandinavia, such that precipitation will tend to fall more often as rain than as snow. 2) Moisture
transport via southern AR implies that the moisture is routed over longer distances across the central
continent before it arrives in Norway. AR traversing the continent can no longer take up significant
amounts of moisture but instead lose moisture via precipitation. By contrast, AR originating from
970 >60°N and crossing the open North Atlantic can take up moisture until they make landfall at the
Norwegian coast. These changes likely account for the lower AR precipitation rates determined along
the western coast of Norway (Fig. 9b).

5 Discussion

975 5.1 Uncertainties with respect to the **global drivingchoice of CMIP5 models**

We now investigate individual ensemble members for a selected set of indices, namely, the changes
in AR days frequency, the annual maximum precipitation, and the contribution of ARs to the yearly
total heavy precipitationClimate models are designed and validated to simulate the mean state and
980 mean variability of the long-term climate. Hence, the validation of climatic extremes during model
development is relatively small. As a result, the models' solutions will differ more for extreme regimes.
Figure 11 shows the inter-model standard deviations for the different percentiles of precipitation. The
percentiles were calculated for all nine models (Table 2) covering the historical period. For the higher
percentiles, the spread over the models clearly increases, such that uncertainties are highest in the
985 extreme precipitation range, i.e., the range where AR precipitation is expected to occur. Therefore, to
assess the uncertainties associated with model choice, in the following we consider the spread in the
ensemble members with respect to ARF, %AMP, and 95P%.

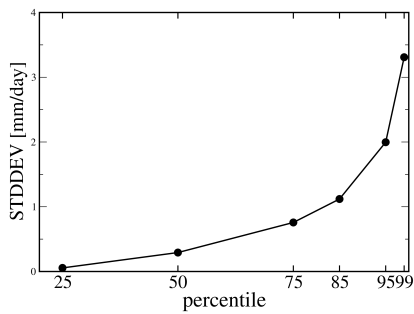


Figure 12: GrossInter-model standard deviation from the nine downscaled models calculated for the 25th, 50th, 75th, 85th, 95th, 99th percentiles of precipitation. The average over all the land grid cells of the models is shown. The percentiles have been derived from the 6-hourly time-series of precipitation.

995 Figure 13a depicts the frequency of ARs. All realizations exhibit a highly coherent spatial pattern which is similar RCA ensemble mean (Fig. 9a) indicating the latter as a representative indicator for the bulk response. The model spread as summarized by the ensemble standard deviation asserts highest uncertainties in two latitudinal bands north of 40 °N and north of 55 °N in the North Atlantic. — for RCA-HAD, RCA-IPSL, and RCA-MPI while RCA-MIROC and RCA-ECE show a particularly weak signal for the RCA realizations. A notably strong increase over the North Atlantic is registered. RCA-ECE show a distinct separation into a northern and southern core zone of increased AR presence. Figure 12a depicts the frequency of AR days. All realizations exhibited a highly coherent spatial pattern that was similar to the RCA ensemble mean (Fig. 8a), indicating the latter as a representative indicator of the bulk response. The uncertainties in the model spread as indicated by the ensemble's standard deviation (Fig. 8a) were highest in the southern UK, France, Belgium, the Netherlands, Luxembourg, and western Iberia. In conclusion, the uncertainty in the response is highest in those regions where AR are frequent already during the historical period (Fig. 5a). RCA-HAD, RCA-CAN, RCA-IPSL and RCA-GFDL showed the strongest response, whereas the response in RCA-MIROC and RCA-ECE was exceptionally weak. The weak climate impact in RCA-MIROC is a direct consequence of low increase in detected AR (~5%, Table 3). Only one single model shows a clear signal along the Norwegian coast (RCA-HAD). Notably, one realization shows wider areas of decreased AR presence in the high latitude Atlantic (RCA-MIROC).

1010 The response of AR forced annual maximum precipitation events is shown in Figure 13b. No clear consistent response is registered over the topographic elevated region of western Norway i.e. the region which is most impacted by ARs in the historical climate (Fig. Error: Reference source not found). Some models show distinct locations with decreased AR impact over Norway (e.g. RCA-MPI, RCA-GFDL, RCA-IPSL) which is probably linked to the aforementioned decrease of ARs arising from >60°N. The most coherent change across the realizations is the more or less strong increase over the western France which in some realizations extends further to the east. However, also in this region local ensemble variability is pronounced and in RCA-ECE even a decrease is seen. precipitation events over a certain region. most heavy. The pronounced ensemble variability is not unexpected.

1020 because the yearly maxima represent the—The response of AR-forced annual maximum precipitation
1025 events (%AMP) is shown in Figure 12b. No clear consistent response was detected over western
Norway, i.e., the region where in the historical climate the %AMP was highest (Fig. 5b). Some models
(RCA-CAN, RCA-MPI, RCA-GFDL, RCA-IPSL) showed distinct locations over Norway where the
impact of AR was smaller, probably linked to the aforementioned decrease in AR arising from >60°N.
The most coherent change across the realizations was the relatively strong increase over western
France, which in some realizations extended further east. However, also in this region the local
ensemble variability was pronounced and in RCA-ECE the %AMP in fact decreased.

1030 Uncertainties with respect to the contribution to the heavy precipitation is budget—highest in the region
of largest changes (Fig. 13c). High inter-model variance is found for the southern tip of Iberia—
indicated by maximal standard deviations. In this region the contribution can either be reduced as in
RCA-HAD or increased as high as +50% as in RCA-CNRM but with a lower magnitude in Italy—
seen likewise. The same change pattern is . . . Higher uncertainties are likewise found for central Europe
(France, Belgium, Netherlands, Germany). In case of This mainly reflects the different inland
penetration of ARs in the models response to climate change. RCA-MIROC and RCA-ECE this results
1035 in only very low change (<5%) for wide regions of France and Germany. With respect to the UK only
one model RCA-HAD shows notable reductions of AR contributions over the UK. Uncertainties with
respect to the contribution to heavy precipitation (%95P) were highest in France and Iberia (Fig. 12c).
High inter-model variation was determined also for the southern tip of Iberia, where the standard
deviations were highest. In this region, the contribution of AR was either reduced, as in RCA-HAD, or
1040 increased by as much as 50%, as in RCA-CNRM. Larger uncertainties were likewise identified for
central Europe (France, Belgium, Netherlands, Germany), with the direction of change being
consistently positive. In RCA-HAD, RCA-CNRM, and RCA-MIROC, the changes over eastern France
and Germany were extremely low. A notable decrease, occurring in the UK; was modeled only by
RCA-HAD.

1045

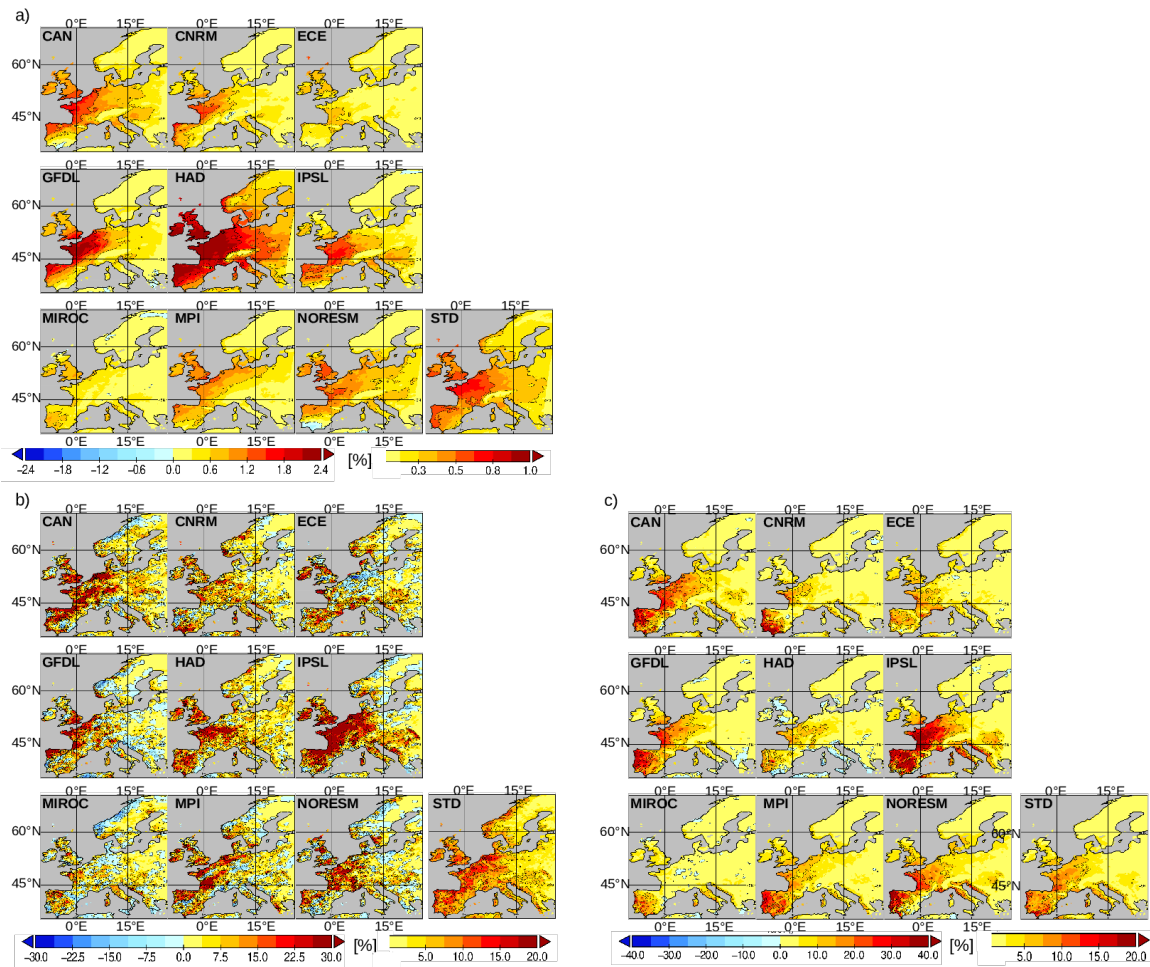


Figure 13: Change in AR day frequency (2070-2099 minus 1970-1999). b) same as a) but for percentage in AR forced yearly maximum precipitation (%AMP); c) same as a) but for AR fractional contribution to heavy precipitation events (>95th percentile). Note the RCA realization are denoted by their forcing global model simply. STD denotes the inter-model standard deviation. Long bars indicate the color scale of the ensemble member indices. Short bars are for inter-model standard deviation.

In summary we can conclude that the ensemble members robustly agree on a stronger future AR impact on heavy precipitation over western-central Europe with a hot spot over NW-France and further extension eastward depending on the realization. In summary, our analysis showed a robust inter-model agreement for the general spatial pattern. However, local uncertainty is high especially in %AMP (i.e. the most severe precipitation events, Fig. 12b), where even the direction of change is not consistent.

5.2 Differences to global projections

Our results generally agree with results from global CMIP5 models (e.g. Gao et al., 2016; Ramos et al., 2016) that ARs become more frequent and intense. With respect to previous studies we note that the climate change effect on AR frequency strongly depends on the chosen reference period. Studies that employ the 85th-percentile threshold derived from the historical period likewise for the future period often find a doubling of AR frequency (e.g. Lavers et al., 2013; Ramos et al., 2016). However, we here calculated separate 85th-percentile thresholds distinctively for historical and future periods. This was done because the 85th-percentile threshold as suggested by Lavers et al. (2012) represents the median-IVT value within observed ARs during the historical period

(Neiman et al., 2008). Consequently, the AR frequency increase found in this study is lower (as IVT thresholds for the future period are higher, Fig. 2) than in the aforementioned studies but still amount to +20–30% increase across the models. Our results generally agree with those of the global CMIP5 models (e.g., Lavers et al., 2013; Gao et al., 2016; Ramos et al., 2016), with both indicating more frequent and more intense AR over Europe. With respect to previous studies, the effect of climate change on AR frequency has been shown to strongly depend on the chosen reference period. Studies that applied the 85th percentile threshold derived from the historical period also to the future period often reported a doubling of the AR frequency (e.g., Lavers et al., 2013, Ramos et al., 2016; Gao et al., 2016). However, as noted above, we calculated separate 85th percentile thresholds for these two periods, and the AR frequency increase was therefore lower (because the IVT thresholds for the future period were higher; Fig. 2) than that in the aforementioned studies but nonetheless 20–30% across the models.

Main differences to global projections arise over Norway and the Iberian Peninsula, i.e. two hotspots of AR impact in Europe. Over Iberia the distribution of AR-related heavy precipitation is clearly modulated by topographic structures, like the Sistema Central Plateau, the Sierra Morena mountains, and the Penibaetic orogenic system. These valleys and ridges lead to zonal bands of high and low increases of AR precipitation over Iberia in the future. Furthermore, our regional ensemble does not indicate a robust climate change signal over Norway. Global CMIP5 models indicate for this region an increase of 10 to 20% in the AR contribution to heavy precipitation events in RCP8.5 (Gao et al., 2016; Fig. 9. therein). In contrast to this, the downscaled ensemble indicates only a weak and not robust response over Norway. The change in the AR percentage of annual maximum precipitation can be negative or positive depending on the global model and thus does not indicate a clear signal (Fig 13b).

(Fig 13c). ensemble members below 5% with the exception of the southwestern top of Norway regional is in all. Likewise, the contribution to heavy precipitation. The main differences with respect to global projections occurred over Norway and the Iberian Peninsula, two hotspots of AR impact in Europe. Over Iberia, the distribution of AR-related heavy precipitation was clearly modulated by topographic structures, including the Sistema Central Plateau, the Sierra Morena mountains, and the Penibaetic orogenic system. These valleys and ridges will lead to zonal bands of high and low increases in AR precipitation over Iberia in the future. Over Norway, our regional ensemble did not predict a robust climate change signal for the frequency of ARF, %AMP, %95P, or %TP (Fig. 8). Global CMIP5 models indicated an increase in the regional %TP and %95P of at least 10–20% according to RCP8.5 (Gao et al., 2016, Fig. 9 therein). In our regional model, %AMP was either negative or positive, depending on the global model, and thus did not yield a clear signal (Fig. 12b).

Our finding that ARs from south of 45°N have an increased presence over Europe in the future high-emission scenario points to larger-scale atmospheric circulation changes. Such change could be related to changes in the low-level Jet stream (Gao et al., 2016) and/or indicate systematic changes in regional weather systems (Pasquier et al., 2018). Our finding that in a future high-emission scenario AR from south of 45°N will be more common over Europe than AR from >60°N points to larger-scale atmospheric circulation in the parent global models. While such changes cannot be analyzed in our limited area model, it can be proposed that they are related to changes in the low-level jet stream.

(Gao et al., 2016) and/or systematic changes in regional weather systems (Pasquier et al., 2018). At least in the southern Hemisphere a poleward shift of ARs has been reported for the recent decades (Ma et al., 2020). The authors suggested internal variations of basin-scale sea surface temperatures as likely reasons.

1110

6. Summary and Conclusions

A high-resolution regional climate model with a resolution of 0.22° was applied to investigate the impact of ARs on Europe. The added value of regionalization was analyzed by a hindcast run to downscale the ERA-Interim reanalysis data set with a resolution 0.75° . The added value is most obvious in topographic elevated areas and in the semi-arid climate zone of southern Europe (Iberia, Italy). In the central and southern part of the Iberian Peninsula the contribution to the regional precipitation budget is strongly modulated by E-W striking topographic signatures. This feature is not seen in ERA-I reanalysis data which shows on the contrary N-S striking gradients with highest precipitation in the west. Generally the AR imprint on analyzed indices in the ERAI data set is lower near the western European coasts but more visible in the distal parts of eastern Europe. A high-resolution regional climate model ensemble with a resolution of 0.22° was created to investigate the impact of AR in Europe. The added value of downscaling was demonstrated by a hindcast that was run to downscale the ERAI reanalysis data set with a resolution of 0.75° . In the central and southern Iberian Peninsula, the contribution of AR to the regional precipitation budget was shown to be strongly affected by prominent E-W topographic signatures. This feature was not seen in the ERAI reanalysis data, which instead showed distinct N-S gradients in which precipitation was highest in the west. Over Iberia, the AR imprint on the analyzed indices in the ERAI data set was weaker but stronger in distant parts of eastern Europe (Fig. 5).

1115

1120

1125

1130

in the downscaled simulation compared to ERAI. Inland less far that ARs penetrate indicates this. The regional climate model is further used to investigate the dynamics of ARs in present and future climate. For this in an ensemble of in total 34 simulations was carried to downscale global climate model scenarios from the CMIP5 suite with a coarse resolution between $1.4 - 3^\circ$. The models were used to downscale three greenhouse gas scenarios (RCP2.6, RCP4.5, and RCP8.5). The regional climate model was further used to investigate AR in present and future climates. Thus, an ensemble of global CMIP5 climate simulations ($1.4 - 3^\circ$ resolution) was downscaled to reach a 0.22° resolution. In total, 34 simulations were carried out for the GHG emission scenarios RCP2.6, RCP4.5, and RCP8.5.

1135

1140

The historical simulations from the regional climate model ensemble are in good agreement with global ERAI reanalysis data set and an ERA-I simulation hindcast run. The regional climate ensemble shows strongest AR impact along near-coastal regions explaining up to 60% of yearly maximum precipitation rates in regions with orographic uplift (e.g. Norway). Orographic uplift to the North Atlantic but unaffected exposed regions with coastlines. In rate AR-related rain events constitute a significant contribution to the total annual yearly rain. Here the impact is largest in semi-arid regions of the Iberian Peninsula and along western Italy. The historical simulations from the regional climate model ensemble were in good agreement with the global ERAI reanalysis data set and the ERAI simulation hindcast run. In the regional climate ensemble, AR had the strongest impact in near-

1145

1150 coastal regions, explaining up to 60% of the yearly maximum precipitation rates in regions with orographic uplift (e.g., Norway). Over Iberia and western France, the fractional contribution of AR to total precipitation (%TP) and heavy precipitation (%95P) was up to 20%, and >40%, respectively.

1155 Our results show ARs become more frequent and have a higher moisture load in a future warmer climate (e.g. Lavers et al., 2013; Warner et al., 2015; Gao et al., 2016; Shields and Kiehl, 2016; Ramos et al., 2016; Shields et al., 2019; Massoud et al., 2019; Massoud et al., 2020; Whan et al., 2020). The potential of ARs to force annual maximum precipitation events increases most prominently over western France (Brittany) and northernmost Spain by up to 20% (RCP8.5). No robust ensemble response was found over Norway.

1160 Our regional high-resolution model allows a spatially more accurate calculation of AR contributions to the local water budget than possible with global earth system models. Over the Iberian Peninsula and western France the contribution of AR forced rain to the total annual precipitation increases by up to 10% as well as it does with respect to the total annual precipitation that falls as heavy precipitation (up to +30%) than mean precipitation rates. The increased AR contribution found for the Iberian Peninsula under contemporaneous climate drying is likely to influence the ground-water recharge which is essential for maintaining ecosystem services and supporting agriculture in this area (e.g. Martos-Rosillo et al., 2015).

1165 er a more important role of ARs in the future climate as AR precipitation rates increase strongly. Furthermore, the well-known dryer mean climate conditions in southern Europe (e.g. Jacob et al., 2014; Kjellström et al., 2018; Gröger et al., 2021a; Christensen et al., 2021) at the end of the century favor

1170 Our results showed that in a future warmer climate AR become more frequent and carry a larger moisture load, consistent with the findings of previous studies (e.g., Lavers et al., 2013; Warner et al., 2015; Gao et al., 2016; Shields and Kiehl, 2016; Ramos et al., 2016; Shields et al., 2016; Shields et al., 2019; Massoud et al., 2019; Whan et al., 2020). The potential of ARs to force annual maximum precipitation events is likely to be highest over western France (Brittany) and northernmost Spain, by up to 20% (RCP8.5), whereas no robust ensemble response was determined over Norway. Our regional high-resolution model thus allows a spatially more accurate calculation of the fractional contributions of AR to the local water budget than is possible with global earth system models. It showed that, in the future, the increase in AR-induced precipitation will be larger than the increase in average precipitation such that the fractional contributions of AR to heavy rain (%95P) and total rain (%TP) will also be larger, increasing by up to 10%, and 30%, respectively.

1175 Our results showed that in a future warmer climate AR become more frequent and carry a larger moisture load, consistent with the findings of previous studies (e.g., Lavers et al., 2013; Warner et al., 2015; Gao et al., 2016; Shields and Kiehl, 2016; Ramos et al., 2016; Shields et al., 2016; Shields et al., 2019; Massoud et al., 2019; Whan et al., 2020). The potential of ARs to force annual maximum precipitation events is likely to be highest over western France (Brittany) and northernmost Spain, by up to 20% (RCP8.5), whereas no robust ensemble response was determined over Norway. Our regional high-resolution model thus allows a spatially more accurate calculation of the fractional contributions of AR to the local water budget than is possible with global earth system models. It showed that, in the future, the increase in AR-induced precipitation will be larger than the increase in average precipitation such that the fractional contributions of AR to heavy rain (%95P) and total rain (%TP) will also be larger, increasing by up to 10%, and 30%, respectively.

1180 Our results showed that in a future warmer climate AR become more frequent and carry a larger moisture load, consistent with the findings of previous studies (e.g., Lavers et al., 2013; Warner et al., 2015; Gao et al., 2016; Shields and Kiehl, 2016; Ramos et al., 2016; Shields et al., 2016; Shields et al., 2019; Massoud et al., 2019; Whan et al., 2020). The potential of ARs to force annual maximum precipitation events is likely to be highest over western France (Brittany) and northernmost Spain, by up to 20% (RCP8.5), whereas no robust ensemble response was determined over Norway. Our regional high-resolution model thus allows a spatially more accurate calculation of the fractional contributions of AR to the local water budget than is possible with global earth system models. It showed that, in the future, the increase in AR-induced precipitation will be larger than the increase in average precipitation such that the fractional contributions of AR to heavy rain (%95P) and total rain (%TP) will also be larger, increasing by up to 10%, and 30%, respectively.

1185 In particular for northern Europe we find a more southern position in the origin of ARs in the future warmer climate compared to the historical period. In turn, this likely affects the path of ARs before arriving Scandinavia as moisture travels over a longer distance over land. This leads to locally decreased precipitation rates over Norway in RCP8.5. Our study also showed that AR day frequencies over Europe will increase over all latitudes along the 10°W meridian, albeit with a larger increase at southern than at northern latitudes. This leads to a higher fractional contribution of AR over Europe from more southern latitudes, which in turn affects the route that AR follow east of 10°W. Since the moisture then travels a longer distance over land, a further uptake of moisture by the AR before it arrives in Norway is prevented. For RCP8.5, this should lead to locally decreased precipitation rates over western Norway. By contrast, during the historical period, a larger share of AR came from >60°N, arriving in Norway directly from the North Atlantic.

1190 Our study also showed that AR day frequencies over Europe will increase over all latitudes along the 10°W meridian, albeit with a larger increase at southern than at northern latitudes. This leads to a higher fractional contribution of AR over Europe from more southern latitudes, which in turn affects the route that AR follow east of 10°W. Since the moisture then travels a longer distance over land, a further uptake of moisture by the AR before it arrives in Norway is prevented. For RCP8.5, this should lead to locally decreased precipitation rates over western Norway. By contrast, during the historical period, a larger share of AR came from >60°N, arriving in Norway directly from the North Atlantic.

1195 Our study clearly demonstrates a larger imprint of ARs in Europe on the regional scale and a more
dominant role of forcing heavy precipitation events with potential risk for flooding under the higher
greenhouse gas scenarios RCP4.5 and RCP8.5. However, under the assumption of the greenhouse
gas scenario RCP2.6 most of the climate-induced changes are not robust which points to the potential
benefit of climate mitigation actions. Elsewhere in Europe, our study clearly demonstrated that, under
1200 the higher GHG emission scenarios RCP4.5 and RCP8.5, a larger imprint of AR on the regional scale
and a larger role of heavy precipitation forcing events with a potential risk for flooding can be
expected. However, under RCP2.6, most of the climate-induced changes are not robust and may thus
be responsive to climate mitigation actions.

1205 Finally, the present assessment of AR dynamics in regional ensembles for Europe must be
considered as a first step since the realized horizontal resolution is still coarse (24 km) and not
explicitly resolves convection. The future trends in regional high resolution modelling will allow
resolutions of only a few kilometers and convection-permitting models will be applied (e.g. Giorgi,
2019; Jacob et al., 2020). This will allow a more thorough investigation of the processes mediating the
1210 response of ARs to climate change and their pathway across Europe. Our regional assessment of the
impact of AR on Europe must be considered as a first step, since the realized horizontal resolution is
coarse (24 km) and does not explicitly resolve convection. The next generation of regional high-
resolution models will improve the resolution to only a few kilometers and allow to resolve convection
(e.g. Giorgi, 2019; Jacob et al., 2020). These advances will allow a more thorough investigation of the
1215 processes mediating the response of AR to climate change and the pathways of AR across Europe.

Acknowledgements

The research presented in this study is part of the Baltic Earth program (Earth System Science for the
Baltic Sea region, see <http://www.baltic.earth>). Regional climate scenario simulations have been
1220 conducted on the Linux clusters Krypton, Bi, Triolith and Tetralith, all operated by the National
Supercomputer Centre in Sweden (<http://www.nsc.liu.se/>). Resources on Triolith and Tetralith were
funded by the Swedish National Infrastructure for Computing (SNIC) (grants SNIC 002/12-25, SNIC
2018/3-280 and SNIC 2019/3-356). The Swedish Civil Contingencies Agency (MSB) and the Swedish
Research Council for Sustainable Development (FORMAS) have contributed funding through the
1225 HydroHazards project (MSB 2019-0651). Additional funding was obtained by the Swedish Research
Council for sustainable development (Formas) through the ClimeMarine project, funded within the
framework of the National Research Programme for Climate (grant no. 2017-01949)

1230 Data availability declaration

The datasets generated during and/or analyzed during the current study are available from the
corresponding author on reasonable request.

Competing interests

1235 The authors declare that they have no conflict of interest.

Code/data availability

Numerical model codes available from the respective literature and corresponding first author. Data to
reproduce results presented in this study are available upon reasonable request.

1240 | **References**

- Albano, C. M., M. D. Dettinger, and C. E. Soulard: Influence of atmospheric rivers on vegetation productivity and fire patterns in the southwestern US. *J. Geophys. Res. Biogeosci.*, **122**, 308–323, <https://doi.org/10.1002/2016JG003608>, 2017
- 1245 | Alfieri, L., Dottori, F., Betts, R., Salamon, P., Feyen, L. (2018), Multi-Model Projections of River Flood Risk in Europe under Global Warming. *Climate*, **6**, 6, doi:[10.3390/cli6010006](https://doi.org/10.3390/cli6010006).
- Alfieri, L., Bisselink, B., Dottori, F., Naumann, G., de Roo, A., Salamon, P., Wyser, K. and Feyen, L. (2017), Global projections of river flood risk in a warmer world. *Earth's Future*, **5**: 171-182.
- 1250 | <https://doi.org/10.1002/2016EF000485>
- Ashley, .R. M., Balmforth, D.J., Saul, A.J., and Blanksby, J.D. (2005), Flooding in the future – predicting climate change, risks and responses in urban areas. *Water Sci Technol* **1**, 52 (5): 265–273. doi: <https://doi.org/10.2166/wst.2005.0142>
- 1255 | [Baldwin, J. W., Atwood, A. R., Vecchi, G. A., & Battisti, D. S. \(2021\). Outsize influence of Central American orography on global climate. *AGU Advances*, **2**, e2020AV000343. <https://doi.org/10.1029/2020AV000343>](https://doi.org/10.1029/2020AV000343)
- 1260 | [Brands, S.: A circulation-based performance atlas of the CMIP5 and 6 models for regional climate studies in the northern hemisphere, *Geosci. Model Dev. Discuss.* \[preprint\], <https://doi.org/10.5194/gmd-2020-418>, in review, 2021](https://doi.org/10.5194/gmd-2020-418)
- 1265 | Cabos, W., de la Vara, A., Álvarez-García, F.J. *et al.* Impact of ocean-atmosphere coupling on regional climate: the Iberian Peninsula case. *Clim Dyn* **54**, 4441–4467 (2020). <https://doi.org/10.1007/s00382-020-05238-x>
- Champeaux, J.L., Masson, V. and Chauvin, F. (2005), ECOCLIMAP: a global database of land surface parameters at 1 km resolution. *Met. Apps*, **12**: 29-32.
- 1270 | <https://doi.org/10.1017/S1350482705001519>
- 1275 | Clarke L, Edmonds J, Jacoby H, Pitcher H, Reilly J, Richels R (2007) Scenarios of greenhouse gas emissions and atmospheric concentrations. Sub-report 2.1A of Synthesis and Assessment Product 2.1 by the U.S. Climate Change Science Program and the Subcommittee on Global Change Research. Department of Energy, Office of Biological & Environmental Research, Washington, 7 DC., USA, pp 154
- 1280 | [Chikhar, K., & Gauthier, P. \(2017\). Impact of Lateral Boundary Conditions on Regional Analyses. *Monthly Weather Review*, **145**\(4\), 1361-1379.](https://doi.org/10.1175/1525-7540(2017)145<1361:ILBCRA>2.0.CO;2)
- Christensen, O.B., Kjellström, E., Dieterich, C., Gröger, M., Meier, H.E.M. (2021). Regional climate projections for the Baltic Sea Region until 2100, *Earth System Dynamics*, [submitted/accepted](https://doi.org/10.5194/egusphere/abstract/2021.1111).
- 1285 | Dacre, H. F., P. A. Clark, O. Martinez-Alvarado, M. A. Stringer, and D. A. Lavers (2015), How do atmospheric rivers form?, *Bull. Am. Meteorol. Soc.*, **96**(8), 1243–1255, <http://dx.doi.org/10.1175/BAMS-D-14-00031.1>

- 1290 [Davies, T. \(2014\), Lateral boundary conditions for limited area models. Q.J.R. Meteorol. Soc., 140: 185-196. https://doi.org/10.1002/qj.2127](https://doi.org/10.1002/qj.2127)
- 1295 [Dee, D.P., Uppala, S.M., Simmons, A.J., Berrisford, P., Poli, P., Kobayashi, S., Andrae, U., Balmaseda, M.A., Balsamo, G., Bauer, P., Bechtold, P., Beljaars, A.C.M., van de Berg, L., Bidlot, J., Bormann, N., Delsol, C., Dragani, R., Fuentes, M., Geer, A.J., Haimberger, L., Healy, S.B., Hersbach, H., Hólm, E.V., Isaksen, I., Kållberg, P., Köhler, M., Matricardi, M., McNally, A.P., Monge-Sanz, B.M., Morcrette, J.-J., Park, B.-K., Peubey, C., de Rosnay, P., Tavolato, C., Thépaut, J.-N. and Vitart, F., The ERA-Interim reanalysis: configuration and performance of the data assimilation system. Q.J.R. Meteorol. Soc., 137: 553-597. https://doi.org/10.1002/qj.828, 2011](https://doi.org/10.1002/qj.828)
- 1300 Dettinger, M. D. (2011), Climate change, atmospheric rivers, and floods in California—A multimodel analysis of storm frequency and magnitude changes. *Journal of the American Water Resources Association*, 47(3), 514–523
- 1305 Dettinger MD. 2013. Atmospheric rivers as drought busters on the U.S. West Coast. *J. Hydrometeor.* 14:1721–32, <https://doi.org/10.1175/JHM-D-13-02.1>
- Dieterich, C., Wang, S., Schimanke, S., Gröger, M., Klein, B., Hordoir, R., Samuelsson, P., Liu, Y., Axell, L., Höglund, A., Meier, H.E.M. (2019a): Surface heat budget over the North Sea in climate change simulations. *Atmosphere*, 10, 272. doi:10.3390/atmos10050272.
- 1310 Dieterich, C. and Gröger, M. and Arneborg, L. and Andersson, H. C., 2019b. Extreme sea levels in the Baltic Sea under climate change scenarios -- Part 1: Model validation and sensitivity, *Ocean Sci*, 15, 6, 1399-1418, 10.5194/os-15-1399-2019
- 1315 Di Luca, A., de Elía, R. & Laprise, R. Potential for added value in precipitation simulated by high-resolution nested Regional Climate Models and observations. *Clim Dyn* **38**, 1229–1247 (2012). <https://doi.org/10.1007/s00382-011-1068-3>
- 1320 Espinoza, V., Waliser, D. E., Guan, B., Lavers, D. A., & Ralph, F. M. (2018). Global analysis of climate change projection effects on atmospheric rivers. *Geophysical Research Letters*, 45, 4299–4308. <https://doi.org/10.1029/2017GL076968>
- 1325 Emori, S., and Brown, S. J. (2005), Dynamic and thermodynamic changes in mean and extreme precipitation under changed climate, *Geophys. Res. Lett.*, 32, L17706, doi:[10.1029/2005GL023272](https://doi.org/10.1029/2005GL023272)
- Feser F. , Rockel B. , von Storch H. , Winterfeldt J. , Zahn R . Regional climate models add value to global model data: a review and selected examples. *Bull. Am. Meteorol. Soc.* 2011; 92(9): 1181–1192. DOI: [10.1175/2011BAMS3061.1](https://doi.org/10.1175/2011BAMS3061.1)
- 1330 Gao, Y., Lu, J., & Leung, L. R. (2016), Uncertainties in Projecting Future Changes in Atmospheric Rivers and Their Impacts on Heavy Precipitation over Europe, *Journal of Climate*, 29(18), 6711-6726; DOI: <https://doi.org/10.1175/JCLI-D-16-0088.1>, 2016.
- 1335 Gimeno L, Nieto R, Vázquez M and Lavers DA (2014) Atmospheric rivers: a mini-review. *Front. Earth Sci.* 2:2. doi: 10.3389/feart.2014.00002
- Gimeno, L., Dominguez, F., Nieu, R., Trigo, R., Drumond, A., Reason, C. J.C., Taschetto, A.S., Ramos, A.M., Kumar, R., Marengo, J., (2016), [Major Mechanisms of Atmospheric Moisture](https://doi.org/10.1002/qj.2828)

[Transport and Their Role in Extreme Precipitation Events](#), Annual Review of Environment and Resources 2016 41:1, 117-141

1340

Giorgi F (2019) Thirty years of regional climate modeling: Where are we and where are we going next? J Geophys Res 124:5696–5723. <https://doi.org/10.1029/2018JD030094>

1345

[Gómez-Navarro, J. J., Montávez, J. P., Jerez, S., Jiménez-Guerrero, P., Lorente-Plazas, R., González-Rouco, J. F., and Zorita, E.: A regional climate simulation over the Iberian Peninsula for the last millennium, Clim. Past, 7, 451–472, https://doi.org/10.5194/cp-7-451-2011, 2011.](#)

1350

Gröger, M., Dieterich, C., Meier, H.E.M., Schimanke, S., (2015) Thermal air–sea coupling in hindcast simulations for the North Sea and Baltic Sea on the NW European shelf, Tellus A: Dynamic Meteorology and Oceanography, 67:1, DOI: 10.3402/tellusa.v67.26911

1355

Gröger, M., Arneborg, L., Dieterich, C., Höglund, A., and Meier, H.E.M. (2019), Summer hydrographic changes in the Baltic Sea, Kattegat and Skagerrak projected in an ensemble of climate scenarios downscaled with a coupled regional ocean–sea ice–atmosphere model. Clim Dyn 53, 5945–5966 doi:10.1007/s00382-019-04908-9

1360

Gröger, M., Dieterich, C., Meier, H.E.M., (2021a), Is interactive air sea coupling relevant for simulating the future climate of Europe?, Climate Dynamics, doi: 10.1007/s00382-020-05489-8, [2021a](#).
[Gröger, M., Dieterich, C., Haapala, J., Ho-Hagemann, H. T. M., Hagemann, S., Jakacki, J., May, W., Meier, H. E. M., Miller, P. A., Rutgersson, A., and Wu, L. \(2021b\): Coupled regional Earth system modelling in the Baltic Sea region, Earth Syst. Dynam. Discuss. \[preprint\], https://doi.org/10.5194/esd-2021-14, in review.](#)

1365

[Guan, B., and Waliser, D. E. \(2015\), Detection of atmospheric rivers: Evaluation and application of an algorithm for global studies, J. Geophys. Res. Atmos., 120, 12514–12535, doi:10.1002/2015JD024257](#)

1370

[Gröger, M., Dieterich, C., Haapala, J., Ho-Hagemann, H. T. M., Hagemann, S., Jakacki, J., May, W., Meier, H. E. M., Miller, P. A., Rutgersson, A., and Wu, L.: Coupled regional Earth system modeling in the Baltic Sea region, Earth Syst. Dynam., 12, 939–973, https://doi.org/10.5194/esd-12-939-2021, 2021b.](#)

1375

Hagemann, S., and L. Dümenil (1998), A parameterization of the lateral waterflow for the global scale, Clim. Dyn., 14, 17– 31

Hagemann, S., H. Göttel, D. Jacob, P. Lorenz, and E. Roeckner (~~2009~~), Improved regional scale processes reflected in projected hydrological changes over large European catchments, Clim. Dyn., 32(6), 767– 781, doi:10.1007/s00382-008-0403-9, [2009](#).

1380

[Harvey, B.J., Shaffrey, L.C. & Woollings, T.J. Equator-to-pole temperature differences and the extra-tropical storm track responses of the CMIP5 climate models. Clim Dyn 43, 1171–1182. https://doi.org/10.1007/s00382-013-1883-9, 2014.](#)

1385

Harvey, B. J., Cook, P., Shaffrey, L. C., & Schiemann, R. (~~2020~~). The response of the northern hemisphere storm tracks and jet streams to climate change in the CMIP3, CMIP5, and CMIP6 climate models. Journal of Geophysical Research: Atmospheres, 125, e2020JD032701. <https://doi.org/10.1029/2020JD032701>, [2020](#).

- 1390 Held IM, Soden BJ (2006) Robust responses of the hydrological cycle to global warming. *J Clim* 19(21):5686–5699, <https://doi.org/10.1175/JCLI3990.1>.
- 1395 [Hohenegger, C., L. Kornblueh, D. Klocke, T. Becker, G. Cioni, J. F. Engels, U. Schulzweida, and B. Stevens, 2020: Climate statistics in global simulations of the atmosphere, from 80 to 2.5 km grid spacing. *J. Meteor. Soc. Japan*, 98, 73-91.](#)
- 1400 Ho-Hagemann, H.T.M., Gröger, M., Rockel, B., Zahn, M., Geyer, B., Meier, H.E.M. (2017): Effects of air-sea coupling over the North Sea and the Baltic Sea on simulated summer precipitation over Central Europe. *Climate Dyn.*, pp. 1–26. doi:10.1007/s00382-017-3546-8.
- 1405 Huang, X., Swain, D.L., and Hall, A.D., 2020, Future precipitation increase from very high resolution ensemble downscaling of extreme atmospheric river storms in California, *Science*, 6, (29), doi: 10.1126/sciadv.aba1323
- 1410 [Ionita, M., Nagavciuc, V., and Guan, B.: Rivers in the sky, flooding on the ground: the role of atmospheric rivers in inland flooding in central Europe. *Hydrol. Earth Syst. Sci.*, 24, 5125–5147., <https://doi.org/10.5194/hess-24-5125-2020>, 2020](#)
- 1415 Jacob, D. (2001), A note to the simulation of the annual and interannual variability of the water budget over the Baltic Sea drainage basin, *Meteorol. Atmos. Phys.*, 77(1–4), 61– 73
- Jacob, D., Petersen, J., Eggert, B. *et al.* EURO-CORDEX (2014): new high-resolution climate change projections for European impact research. *Reg Environ Change* **14**, 563–578. <https://doi.org/10.1007/s10113-013-0499-2>
- 1420 Jacob D, Teichmann C, Sobolowski S et al (2020) Regional climate downscaling over Europe: perspectives from the EURO-CORDEX community. *Reg Environ Change*. <https://doi.org/10.1007/s10113-020-01606-9>.
- 1425 Jeworrek J, Wu L, Dieterich C, Rutgersson A (2017) Characteristics of convective snow bands along the Swedish east coast. *Earth Syst Dyn* 8:163–175. <https://doi.org/10.5194/esd-8-163-2017>
- Jungclaus, J. H., N. Fischer, H. Haak, K. Lohmann, J. Marotzke, D. Matei, U. Mikolajewicz, D. Notz, and J. S. von Storch (2013), Characteristics of the ocean simulations in MPIOM, the ocean component of the MPI-Earth system model, *J. Adv. Model. Earth Syst.*, 5, 422– 446, doi:10.1002/jame.20023
- 1430 Kaiser-Weiss, A.K., Borsche, M., Niermann, D., Kaspar, F., Lussana, C., Isotta, F.A., van den Besselaar, E., van der Schrier, G., and Unden, P., (2019), Added value of regional reanalyses for climatological applications, *Environ. Res. Commun.* <https://doi.org/10.1088/2515-7620/ab2ec3>
- Kelemen, F.D., Primo, C., Feldmann, H., Ahrens, B. (2019), Added Value of Atmosphere-Ocean Coupling in a Century-Long Regional Climate Simulation, *Atmosphere*, 10(9), 537, <https://doi.org/10.3390/atmos10090537>.

- 1435 Kjellström, E., Nikulin, G., Strandberg, G., Christensen, O. B., Jacob, D., Keuler, K., Lenderink, G., van Meijgaard, E., Schär, C., Somot, S., Sørland, S. L., Teichmann, C., and Vautard, R. (2018), European climate change at global mean temperature increases of 1.5 and 2°C above pre-industrial conditions as simulated by the EURO-CORDEX regional climate models, *Earth Syst. Dyn.*, 9, 459–
- 1440 478, <https://doi.org/10.5194/esd-9-459-2018>.
- Kousky C (2014) Informing climate adaptation: a review of the economic costs of natural disasters. *Energy Econ* 46:576–592, <https://doi.org/10.1016/j.eneco.2013.09.029>.
- 1445 Kupiainen M. , Jansson C. , Samuelsson P. , Jones C. , Willén U. , co-authors . Rossby Centre regional atmospheric model, RCA4, Rossby Center News Letter. 2014. Online at: <http://www.smhi.se/en/Research/Research-departments/climate-research-rossby-centre2-552/1.16562> .
- 1450 Lavers, D. A., R. P. Allan, E. F. Wood, G. Villarini, D. J. Brayshaw, and A. J. Wade (2011), Winter floods in Britain are connected to atmospheric rivers, *Geophys. Res. Lett.*, 38, L23803, doi:10.1029/2011GL049783, 2011
- 1455 Lavers, D. A., G. Villarini, R. P. Allan, E. F. Wood, and A. J. Wade (2012), The detection of atmospheric rivers in atmospheric reanalyses and their links to British winter floods and the large-scale climatic circulation, *J. Geophys. Res.*, 117, D20106, doi:10.1029/2012JD018027, 2012
- Lavers, D. A., and Villarini, G. (2013), The nexus between atmospheric rivers and extreme precipitation across Europe, *Geophys. Res. Lett.*, 40, 3259– 3264, doi:10.1002/grl.50636, 2013
- 1460 Lavers, D. A. & Villarini, G. (2015), The contribution of atmospheric rivers to precipitation in Europe and the United States. *J. Hydrol.* 522, 382–390, 2015.
- 1465 Lavers, D. A., Allan, R.P., Villarini, G., Lloyd-Hughes, B., Brayshaw, D.J., Wade, A.J. (2013), Future changes in atmospheric rivers and their implications for winter flooding in Britain, *Environ. Res. Lett.* 8, 034010, DOI: 10.1088/1748-9326/8/3/034010, 2013
- 1470 Lavers, D. A., R. P. Allan, E. F. Wood, G. Villarini, D. J. Brayshaw, and A. J. Wade (2011), Winter floods in Britain are connected to atmospheric rivers, *Geophys. Res. Lett.*, 38, L23803, doi:10.1029/2011GL049783.
- Lavers, D. A., Ralph, F. M., Waliser, D. E., Gershunov, A., and Dettinger, M. D. (2015), Climate change intensification of horizontal water vapor transport in CMIP5, *Geophys. Res. Lett.*, 42, 5617–5625, doi:10.1002/2015GL064672
- 1475 Ma, W., Chen, G., & Guan, B. (2020). Poleward shift of atmospheric rivers in the Southern Hemisphere in recent decades. *Geophysical Research Letters*, 47, e2020GL089934. <https://doi.org/10.1029/2020GL089934>
- 1480 Madec G, The NEMO Team (2012) "NEMO ocean engine": Note du Pole de modélisation de l'Institut Pierre-Simon Laplace, France, No 27, ISSN no 1288-1619
- Marsland, S. J., H. Haak, J. H. Jungclaus, M. Latif, and F. Roeske (2002), The Max-Planck-Institute global ocean/sea ice model with orthogonal curvilinear coordinates, *Ocean Modell.*, 5(2), 91– 126

- 1485 Martos-Rosillo, S., González-Ramón, A., Jiménez-Gavilán, P. *et al.* Review on groundwater recharge in carbonate aquifers from SW Mediterranean (Betic Cordillera, S Spain). *Environ Earth Sci* **74**, 7571–7581 (2015). <https://doi.org/10.1007/s12665-015-4673-3>, 2015.
- 1490 Massoud, E.; Massoud, T.; Guan, B.; Sengupta, A.; Espinoza, V.; De Luna, M.; Raymond, C. (2020); Waliser, D. Atmospheric Rivers and Precipitation in the Middle East and North Africa (MENA). *Water*, **12**, 2863. <https://doi.org/10.3390/w12102863> Massoud, E. C., H., Lee, P. B., Gibson, P., Loikith, and D. E., Waliser: Bayesian Model Averaging of Climate Model Projections Constrained by Precipitation Observations over the Contiguous United States, *Journal of Hydrometeorology*, **21**, 2401-2418. <https://doi.org/10.1175/JHM-D-19-0258.1>, 2020.
- 1495 Massoud, E. C., Espinoza, V., Guan, B., & Waliser, D. E. (2019). Global Climate Model Ensemble Approaches for Future Projections of Atmospheric Rivers. *Earth's Future*, **7**: 1136– 1151. <https://doi.org/10.1029/2019EF001249>
- 1500 Nayak, M. A., and Villarini, G. (2017), A long-term perspective of the hydroclimatological impacts of atmospheric rivers over the central United States, *Water Resour. Res.*, **53**, 1144– 1166, doi:[10.1002/2016WR019033](https://doi.org/10.1002/2016WR019033)
- 1505 Nayak, M. A., G. Villarini, and A. A. Bradley (2016), Atmospheric rivers and rainfall during NASA's Iowa Flood Studies (IFloodS) Campaign, *J. Hydrometeorol.*, **17**(1), 257– 271
- Nayak, M. A., G. Villarini, and D. A. Lavers (2014), On the skill of numerical weather prediction models to forecast atmospheric rivers over the central United States, *Geophys. Res. Lett.*, **41**, 4354–4362, doi:[10.1002/2014GL060299](https://doi.org/10.1002/2014GL060299)
- 1510 Neiman, P. J., , F. M. Ralph, , G. A. Wick, , J. D. Lundquist, , and M. D. Dettinger, 2008: Meteorological characteristics and overland precipitation impacts of atmospheric rivers affecting the west coast of North America based on eight years of SSM/I satellite observations. *J. Hydrometeorol.*, **9**, 22–47, doi:[10.1175/2007JHM855.1](https://doi.org/10.1175/2007JHM855.1).
- 1515 Neiman, P. J., L. J. Schick, F. M. Ralph, M. Hughes, and G. A. Wick (2011), Flooding in Western Washington: The connection to atmospheric rivers, *J. Hydrometeorol.*, **12**(6), 1337–1358
- 1520 O'Brien, T. A., Payne, A. E., Shields, C. A., Rutz, J., Brands, S., Castellano, C., Chen, J., Cleveland, W., DeFlorio, M. J., Goldenson, N., Gorodetskaya, I. V., Díaz, H. I., Kashinath, K., Kawzenuk, B., Kim, S., Krinitskiy, M., Lora, J. M., McClenny, B., Michaelis, A., O'Brien, J. P., Patricola, C. M., Ramos, A. M., Shearer, E. J., Tung, W., Ullrich, P. A., Wehner, M. F., Yang, K., Zhang, R., Zhang, Z., & Zhou, Y. (2020). Detection Uncertainty Matters for Understanding Atmospheric Rivers, *Bulletin of the American Meteorological Society*, **101**(6), E790-E796
- 1525 Pasquier, J. T., Pfahl, S., & Grams, C. M. (2019). Modulation of atmospheric river occurrence and associated precipitation extremes in the North Atlantic Region by European weather regimes. *Geophysical Research Letters*, **46**, 1014– 1023. <https://doi.org/10.1029/2018GL081194>
- 1530 Payne, A.E., Demory, ME., Leung, L.R. *et al.* (2020), Responses and impacts of atmospheric rivers to climate change. *Nat Rev Earth Environ* **1**, 143–157, <https://doi.org/10.1038/s43017-020-0030-5>
- Primo, C., Kelemen, F. D., Feldmann, H., Ahrens, B. (2019): A regional atmosphere-ocean climate system model (CCLMv5.0clm7-NEMOv3.3-NEMOv3.6) over Europe including three marginal seas: on

- 1535 its stability and performance, *Geoscientific Model Development Discussions*, 2019, 1-33, doi: 10.5194/gmd-2019-73
- Ralph, F. M., P. J. Neiman, G. A. Wick, S. I. Gutman, M. D. Dettinger, D. R. Cayan, and A. B. White (2006), Flooding on California's Russian River: Role of atmospheric rivers, *Geophys. Res. Lett.*, 33, L13801, doi:10.1029/2006GL026689.
- 1540 Ralph FM, Dettinger MD. 2011. Storms, floods, and the science of atmospheric rivers. *EOS* 92(32):265–66
- 1545 Ralph, F. M., and M. D. Dettinger (2012), Historical and national perspectives on extreme West Coast precipitation associated with atmospheric rivers during December 2010, *Bull. Am. Meteorol. Soc.*, 93, 783–790, doi:10.1175/BAMS-D-11-00188.1.
- Ramos AM, Trigo RM, Liberato MLR, Tomé R. 2015a Daily precipitation extreme events in the Iberian Peninsula and its association with atmospheric rivers. *J. Hydrometeor.* 16:579–97
- 1550 Ramos, A. M., Nieto, R., Tomé, R., Gimeno, L., Trigo, R. M., Liberato, M. L. R., and Lavers, D. A (2016): Atmospheric rivers moisture sources from a Lagrangian perspective, *Earth Syst. Dynam.*, 7, 371–384, <https://doi.org/10.5194/esd-7-371-2016>, 2016a
- 1555 Ramos, A. M., R. Tomé, R. M. Trigo, M. L. R. Liberato, and J. G. Pinto (2016), Projected changes in atmospheric rivers affecting Europe in CMIP5 models, *Geophys. Res. Lett.*, 43, 9315–9323, doi:10.1002/2016GL070634
- 1560 Riahi K, Gruebler A, Nakicenovic N (2007) Scenarios of long-term socio-economic and environmental development under climate stabilization. *Technol Forecast Soc Chang* 74(7):887–935
- Riahi K, Rao S, Krey V et al (2011) RCP 8.5—a scenario of comparatively high greenhouse gas emissions. *Clim Change* 109:33. <https://doi.org/10.1007/s10584-011-0149-y>
- 1565 Samuelsson P, Jones CG, Willen U, Ullerstig A, Golvig S, Hansson U, Jansson C, Kjellström E, Nikulin G, Wyser K (2011) The Rossby Centre Regional Climate model RCA3: model description and performance. *Tellus A* 63:4–23. <https://doi.org/10.1111/j.1600-0870.2010.00478.x>
- 1570 Sayers, P.B; Horritt, M; Penning-Rowsell, E; McKenzie, A. (2015) *Climate Change Risk Assessment 2017: Projections of future flood risk in the UK*. Research undertaken by Sayers and Partners on behalf of the Committee on Climate Change. Published by Committee on Climate Change, London.
- 1575 [Shields, C. A., and Kiehl, J. T. \(2016\). Simulating the Pineapple Express in the half degree Community Climate System Model, CCSM4, *Geophys. Res. Lett.*, 43, 7767– 7773, doi:10.1002/2016GL069476](#)
- 1580 Schiemann, R., Vidale, P. L., Shaffrey, L. C., Johnson, S. J., Roberts, M. J., Demory, M.-E., Mizielinski, M. S., and Strachan, J. (2018): Mean and extreme precipitation over European river basins better simulated in a 25 km AGCM, *Hydrol. Earth Syst. Sci.*, 22, 3933–3950, <https://doi.org/10.5194/hess-22-3933-2018>.
- Sein, D. V., Mikolajewicz, U., Gröger, M., Fast, I., Cabos, W., Pinto, J. G., et al. (2015). Regionally coupled atmosphere-ocean-sea ice-marine biogeochemistry model ROM: 1. description and validation. *J. Adv. Model. Earth Syst.* 7, 268–304. doi: 10.1002/2014ms000357

- 1585 Sein, D.V, Gröger, M., Cabos, W., Alvarez, F., Hagemann, S., de la Vara, A., Pinto, J.G., Izquierdo, A., Koldunov, N.V., Dvornikov, A. Y., Limareva, N., Martinez, B., Jacob, D. (2020), Regionally coupled atmosphere - ocean - marine biogeochemistry model ROM: 2. Studying the climate change signal in the North Atlantic and Europe J. Adv. Model. Earth Syst., <https://doi.org/10.1029/2019MS001646>.
- 1590 Sodemann, H. & Stohl, A. (2013), Moisture origin and meridional transport in atmospheric rivers and their association with multiple cyclones. *Mon. Weather Rev.* **141**, 2850–2868
- 1595 Soto-Navarro, J., Jordá, G., Amores, A. et al. Evolution of Mediterranean Sea water properties under climate change scenarios in the Med-CORDEX ensemble. *Clim Dyn* 54, 2135–2165 (2020). <https://doi.org/10.1007/s00382-019-05105-4>
- 1600 Shields, C. A., and Kiehl, J. T. (2016), Atmospheric river landfall-latitude changes in future climate simulations, *Geophys. Res. Lett.*, 43, 8775– 8782, doi:[10.1002/2016GL070470](https://doi.org/10.1002/2016GL070470), 2016.
- 1605 [Shields, C. A., Rutz, J. J., Leung, L.-Y., Ralph, F. M., Wehner, M., Kawzenuk, B., Lora, J. M., McClenny, E., Osborne, T., Payne, A. E., Ullrich, P., Gershunov, A., Goldenson, N., Guan, B., Qian, Y., Ramos, A. M., Sarangi, C., Sellars, S., Gorodetskaya, I., Kashinath, K., Kurlin, V., Mahoney, K., Muszynski, G., Pierce, R., Subramanian, A. C., Tome, R., Waliser, D., Walton, D., Wick, G., Wilson, A., Lavers, D., Prabhat, Collow, A., Krishnan, H., Magnusdottir, G., and Nguyen, P.: Atmospheric River Tracking Method Intercomparison Project \(ARTMIP\): project goals and experimental design, *Geosci. Model Dev.*, 11, 2455–2474, <https://doi.org/10.5194/gmd-11-2455-2018>, 2018.](https://doi.org/10.1029/2018GL078470)
- 1610 Shields, C. A., Rosenbloom, N., Bates, S., Hannay, C., Hu, A., Payne, A. E., et al. ~~(2019)~~ Meridional heat transport during atmospheric rivers in high-resolution CESM climate projections. *Geophysical Research Letters*, 46, 14702– 14712. <https://doi.org/10.1029/2019GL085565>, 2019
- 1615 [Stevens, B., and Coauthors, The added value of large-eddy and storm-resolving models for simulating clouds and precipitation. *J. Meteor. Soc. Japan*, 98, 395–435, <https://doi.org/10.2151/jmsj.2020-021>, 2020](https://doi.org/10.1029/2020GL028021)
- 1620 Taylor, K.E., Stouffer, R.J., and Meehl, G.A., ~~(2012)~~: An overview of CMIP5 and the experiment design. *Bull Am Meteorol Soc* 93:485–498, 2012
- 1625 [Teichmann C, Bülow K, Otto J, Pfeifer S, Rechid D, Sieck K, Jacob D \(2018\) Avoiding extremes: benefits of staying below +1.5 °C compared to +2.0 °C and +3.0 °C global warming. *Atmosphere* 9:115. <https://doi.org/10.3390/atmos9040115>](https://doi.org/10.1029/2018GL078470)
- 1630 Valcke, S., A. Caubel, D. Declat, and L. Terray (2003), OASIS3 Ocean Atmosphere Sea Ice Soil User's Guide, Tech. Rep. TR/CMGC/03-69, CERFACS, Toulouse, France
- Vancoppenolle, M., Fichefet, T., Goosse, H., Bouillon, S., Madec, G., and Morales Maqueda, M. A. (2008): Simulating the mass balance and salinity of Arctic and Antarctic sea ice. 1. Model description and validation, *Ocean Modell.*, 27, 33–53, doi:10.1016/j.ocemod.2008.10.005.
- van Haren, R., Haarsma, R. J., van Oldenborgh, G. J. & Hazeleger, W. Resolution dependence of European precipitation in a state-of-the-art atmospheric general circulation model (2015), *J. Clim.* 28, 5134–5149.

- 1635 van Vuuren D, den Elzen M, Lucas P, Eickhout B, Strengers B, van Ruijven B, Wonink S, van Houdt R (2007) Stabilizing greenhouse gas concentrations at low levels: an assessment of reduction strategies and costs. *Clim Change*. <https://doi.org/10.1007/s10584-006-9172-9>
- 1640 van Vuuren DP, Stehfest E, den Elzen MGJ et al (2011) RCP2.6: exploring the possibility to keep global mean temperature increase below 2 °C. *Clim Change* 109:95. <https://doi.org/10.1007/s10584-011-0152-3>
- 1645 Wang S., Dieterich C., Döscher R., Höglund A., Hordoir R., Meier HEM, Samuelsson P., Schimanke S., (2015) Development and evaluation of a new regional coupled atmosphere–ocean model in the North Sea and Baltic Sea. *Tellus A* 67:1. <https://doi.org/10.3402/tellusa.v67.24284>
- 1650 Wang X, Li J, Sun C, Liu T (2017) NAO and its relationship with the Northern Hemisphere mean surface temperature in CMIP5 simulations. *J Geophys Res Atmos* 122:4202–4227. <https://doi.org/10.1002/2016JD025979>
- 1655 Warner, M. D., C. F. Mass, and E. P. Salathe (2015), Changes in winter atmospheric rivers along the North American west coast in CMIP5 climate models, *J. Hydrol. Meteorol.*, doi: 10.1175/JHM-D-14-0080.1
- 1660 Whan, K., Sillmann, J., Schaller, N. *et al.* Future changes in atmospheric rivers and extreme precipitation in Norway. *Clim Dyn* **54**, 2071–2084 (2020). <https://doi.org/10.1007/s00382-019-05099-z>
- 1665 Wootten AM, Massoud EC, Sengupta A, Waliser DE, Lee H. The Effect of Statistical Downscaling on the Weighting of Multi-Model Ensembles of Precipitation. *Climate*. 2020; 8(12):138. <https://doi.org/10.3390/cli8120138>
- 1660 Zappa G, Shaffrey LC, Hodges KI (2013) The ability of CMIP5 models to simulate North Atlantic extratropical cyclones. *J Clim* 26(15):5379–5396
- 1665 Zhu, Y., and Newell, R. (1998). A proposed algorithm for moisture fluxes from atmospheric rivers. *Mon. Wea. Rev.* 126, 725–735. doi: 10.1175/1520-0493(1998)126%3C0725:APAFMF%3E2.0.CO;2
- 1670 Zhu, S., Remedio, A.R.C., Sein, D.V. et al. Added value of the regionally coupled model ROM in the East Asian summer monsoon modeling. *Theor Appl Climatol* 140, 375–387 (2020). <https://doi.org/10.1007/s00704-020-03093-8>.